Ore Geology Reviews 71 (2015) 484–501

Contents lists available at ScienceDirect

Ore Geology Reviews

journal homepage: www.elsevier.com/locate/oregeorev

Prospectivity for epithermal gold–silver deposits in the Deseado Massif, Argentina

Pablo Andrada de Palomera [a,b,*], Frank J.A. van Ruitenbeek [a], Emmanuel John M. Carranza [c]

[a] Faculty of Geo-Information Science and Earth Observation (ITC), University of Twente, Enschede, The Netherlands
[b] Fomicruz S.E. Alberdi 643, 9400 Río Gallegos, Santa Cruz, Argentina
[c] School of Earth and Environmental Sciences, James Cook University, Townsville, Queensland, Australia

ARTICLE INFO

Article history:
Received 3 July 2014
Received in revised form 1 December 2014
Accepted 8 December 2014
Available online 13 December 2014

Keywords:
Mineral prospectivity
Epithermal deposits
Deseado Massif
Weights-of-evidence
Mineral exploration

ABSTRACT

Previous prospectivity modelling for epithermal Au–Ag deposits in the Deseado Massif, southern Argentina, provided regional-scale prospectivity maps that were of limited help in guiding exploration activities within districts or smaller areas, because of their low level of detail. Because several districts in the Deseado Massif still need to be explored, prospectivity maps produced with higher detail would be more helpful for exploration in this region. We mapped prospectivity for low- and intermediate-sulfidation epithermal deposits (LISEDs) in the Deseado Massif at both regional and district scales, producing two different prospectivity models, one at regional scale and the other at district-scale. The models were obtained from two datasets of geological evidence layers by the weights-of-evidence (WofE) method. We used more deposits than in previous studies, and we applied the leave-one-out cross validation (LOOCV) method, which allowed using all deposits for training and validating the models. To ensure statistical robustness, the regional and district-scale models were selected amongst six combinations of geological evidence layers based on results from conditional independence tests.

The regional-scale model (1000 m spatial resolution), was generated with readily available data, including a lithological layer with limited detail and accuracy, a clay alteration layer derived from a Landsat 5/7 band ratio, and a map of proximity to regional-scale structures. The district-scale model (100 m spatial resolution) was generated from evidence layers that were more detailed, accurate and diverse than the regional-scale layers. They were also more cumbersome to process and combine to cover large areas. The evidence layers included clay alteration and silica abundance derived from ASTER data, and a map of lineament densities. The use of these evidence layers was restricted to areas of favourable lithologies, which were derived from a geological map of higher detail and accuracy than the one used for the regional-scale prospectivity mapping.

The two prospectivity models were compared and their suitability for prediction of the prospectivity in the district-scale area was determined. During the modelling process, the spatial association of the different types of evidence and the mineral deposits were calculated. Based on these results the relative importance of the different evidence layers could be determined. It could be inferred which type of geological evidence could potentially improve the modelling results by additional investigation and better representation.

We conclude that prospectivity mapping for LISEDs at regional and district-scales were successfully carried out by using WofE and LOOCV methods. Our regional-scale prospectivity model was better than previous prospectivity models of the Deseado Massif. Our district-scale prospectivity model showed to be more effective, reliable and useful than the regional-scale model for mapping at district level. This resulted from the use of higher resolution evidential layers, higher detail and accuracy of the geological maps, and the application of ASTER data instead of Landsat ETM + data. District-scale prospectivity mapping could be further improved by: a) a more accurate determination of the age of mineralization relative to that of lithological units in the districts; b) more accurate and detailed mapping of the favourable units than what is currently available; c) a better understanding of the relationships between LISEDs and the geological evidence used in this research, in particular the relationship with hydrothermal clay alteration, and the method of detection of the clay minerals; and d) inclusion of other data layers, such as geochemistry and geophysics, that have not been used in this study.

1. Introduction

The Deseado Massif in southern Argentina has been explored for epithermal Au–Ag deposits because of its favourable geological setting

* Corresponding author at: Fomicruz S.E. Alberdi 643, 9400 Río Gallegos, Santa Cruz, Argentina. Tel.: +54 2966 429661.
E-mail address: pandrada@fomicruz.com (P. Andrada de Palomera).

http://dx.doi.org/10.1016/j.oregeorev.2014.12.007
0169-1368/

for this type of deposits (Schalamuk et al., 1997, 2002). The exploration activities resulted in the discovery of several new epithermal deposits, of which five have undergone mining, namely Cerro Vanguardia (Zubia et al., 1999), Manantial Espejo (Echeveste, 2010), Mina Marta (Páez et al., 2011), San José (Dietrich et al., 2012), and Lomada de Leiva (Sandefur, 2007). Other deposits are in advanced stages of exploration, such as Cerro Negro (Shatwell et al., 2011), Cerro Moro (Coupland, 2009), La Josefina (Andrada de Palomera et al., 2012; Schalamuk et al., 1999), El Dorado-Monserrat (Echavarría, 2004; Echavarría et al., 2005), and Bajo Pobre (Schalamuk et al., 1997; Zubia and Genini, 2003).

Identification of exploration targets by mineral prospecting often includes reviews of available information, interpretation of remote sensing data, geological mapping, and geochemical and geophysical surveys (Marjoribanks, 2010; Moon et al., 2006); and more recently, GIS-based mapping of mineral prospectivity (e.g., Behnia, 2007; Boleneus et al., 2001; Carranza and Sadeghi, 2010; Ford and Hart, 2013; González-Álvarez et al., 2010; Nykänen and Ojala, 2007; Porwal et al., 2010; Raines, 1999). GIS-based methods convey objectivity and reproducibility, making them useful for assigning priorities to exploration targets, helping with the assessment of different types of geological evidence, and justifying the need of additional investigation.

There are different GIS-based methods for mapping mineral prospectivity, these include logistic regression (Harris and Pan, 1999), the use of evidential belief functions (Carranza and Hale, 2003), fuzzy logic (Carranza and Hale, 2001; Porwal et al., 2003), neural network techniques (Singer and Kouda, 1999), weights-of-evidence modelling (Bonham-Carter et al., 1989), and Bayesian network classifiers (Porwal et al., 2006). Weights-of-evidence (WofE) technique is transparent and easy to interpret compared to alternative methods, such as neural networks, neuro-fuzzy, and Bayesian network classifiers (Agterberg, 2011; Agterberg and Cheng, 2002; Bonham-Carter et al., 1989; Ford and Hart, 2013; Porwal et al., 2010). Logistic regression is computationally intensive and its regression coefficients are hard to interpret (Deng, 2009), and although weighted logistic regression produces unbiased probabilities, its coefficients generally have relatively large variances (Agterberg, 2011). Fuzzy logic allows the use of multiclass variables but, up to a certain degree, it depends on reliable and correct exploration models. WofE is considered to provide conservative estimates and is suitable for areas that are only partially studied (de Quadros et al., 2006). In addition, WofE allows using zero weights for unknown or missing data, avoiding the exclusion of some layers of evidence, as in logistic regressions (Agterberg, 2011; Bonham-Carter et al., 1989; Deng, 2009).

A limitation of WofE is the requirement for conditional independence (CI) between layers of evidence. If this requirement is violated, then bias of estimated probabilities will result (Agterberg, 2011). In general, the bias leads to overestimation of probabilities. The degradation of performance increases with the number of predictor variables (Singer and Kouda, 1999). Therefore, the assumption of conditional independence should be tested when applying WofE modelling (Bonham-Carter et al., 1989).

In the Deseado Massif, regional-scale GIS-based favourability mapping of low-sulfidation epithermal deposits was tested by Carranza and Andrada de Palomera (2005) by using *evidential belief functions* and a limited number of training deposits. Their resultant regional-scale prospectivity maps provided limited help in guiding exploration within districts or smaller areas, partially because of their low level of detail. Prospectivity maps produced with higher detail and adequate effectiveness will be more helpful in guiding the exploration in those areas, and prospectivity mapping in the Deseado Massif could be improved by acquiring the most relevant types of geological evidence for the epithermal deposits being sought and representing them by the most suitable layers of evidence.

This study has three main objectives: (a) to map prospectivity of low- and intermediate-sulfidation epithermal deposits (LISEDs) in the Deseado Massif by training models with most deposits currently known in the region; (b) to test whether more detailed and diverse geological evidence can improve prospectivity mapping, particularly at district-scale; and (c) to determine the types of evidence that should be investigated further to improve prospectivity mapping in the Deseado Massif, mainly at district or larger scales. To reach these objectives, the GIS-based WofE method, and the leave-one-out cross validation method (LOOCV) were applied to two datasets with different levels of detail. The results of mapping with each dataset were compared, and the contributions of different types of evidence to the models' predictions were assessed to determine the types of evidence that need further investigation to improve prospectivity.

2. Geology and epithermal mineralization of the Deseado Massif

2.1. Stratigraphy of the Deseado Massif

The oldest rocks in the Deseado Massif (Fig. 1) belong to the La Modesta Formation of Upper Precambrian to Lower Paleozoic age (Schalamuk et al., 2002). These include schists, phyllites, slates, quartzites, gneisses, and amphibolites, which are intruded by granitic and tonalitic rocks with ductile to ductile–fragile deformation (Giacosa et al., 2002; Ramos, 2002a). The formation is unconformably overlain by continental sediments of the La Golondrina, La Juanita, and El Tranquilo Formations. The Permian La Golondrina and La Juanita Formations include quartz-feldspathic sandstones, siltstones, lithic sandstones, and conglomerates. These are present only in the eastern part of the Deseado Massif (Fig. 1). The El Tranquilo Formation of Middle or Upper Triassic age (De Giusto et al., 1980) consists of alternating fine- to coarse-grained quartz sandstones, shales, fine-grained conglomerates (Sanders, 2000), and intercalations of syn-sedimentary volcanic materials.

During the Lower Jurassic, after the deposition of the El Tranquilo Formation, I-type granitic rocks of the La Leona Formation were intruded in the NE of the region (Márquez et al., 2002; Varela et al., 1991). These rocks are calc-alkaline granodiorites, granites, adamellites, tonalites and diorites (Godeas, 1985). During the remainder of the Jurassic, abundant pyroclastic materials corresponding to the Roca Blanca, Bajo Pobre, Chon Aike, and La Matilde Formations were deposited. These formations filled NNW-trending grabens produced by the generalized extension that broke-up Gondwanaland.

The Roca Blanca Formation of Lower Jurassic (Liassic) age comprises a sub-aerial sequence of tuffs, sandstones, mudstones and volcanoclastic–sedimentary rocks. It has a maximum thickness of 900 m (Panza, 1982) and was deposited in active rift basins (Sanders, 2000).

The Bajo Pobre Formation of middle Jurassic age is composed of predominant porphyritic to aphanitic olivine basalts, subordinate porphyritic andesites and basaltic agglomerates, and minor mafic tuffs, conglomerates and sandstones (Sanders, 2000). Its thickness varies from 150 to 200 m in most outcrops, but locally reaches up to 600 m (Panza, 1994a). Related to the magmatic episode that produced the Bajo Pobre Formation, hypabyssal porphyritic andesites of the Cerro Leon Formation intruded the El Tranquilo, Bajo Pobre and Roca Blanca Formations (Panza, 1982). These are likely intrusive equivalents of the Bajo Pobre Formation (de Barrio et al., 1999; Jovic et al., 2011), and are covered unconformably by the Bahía Laura Group.

During the Middle to Upper Jurassic, rocks of the Bahía Laura Group (Feruglio, 1949; Lesta and Ferello, 1972) formed a pyroclastic volcanic–sedimentary complex of predominantly rhyolitic and partly dacitic composition. The volcanism that produced the Bahía Laura Group probably lasted for about 50 Ma (Schalamuk et al., 1999); having radiometric ages of 177–125 Ma. However, the age of the Bahía Laura Group in relation to the Bajo Pobre Formation is controversial, and radiometric ages of these two units, obtained in different sectors of the Deseado Massif, show some overlap. The Bahía Laura Group is composed of the Chon Aike and La Matilde Formations.

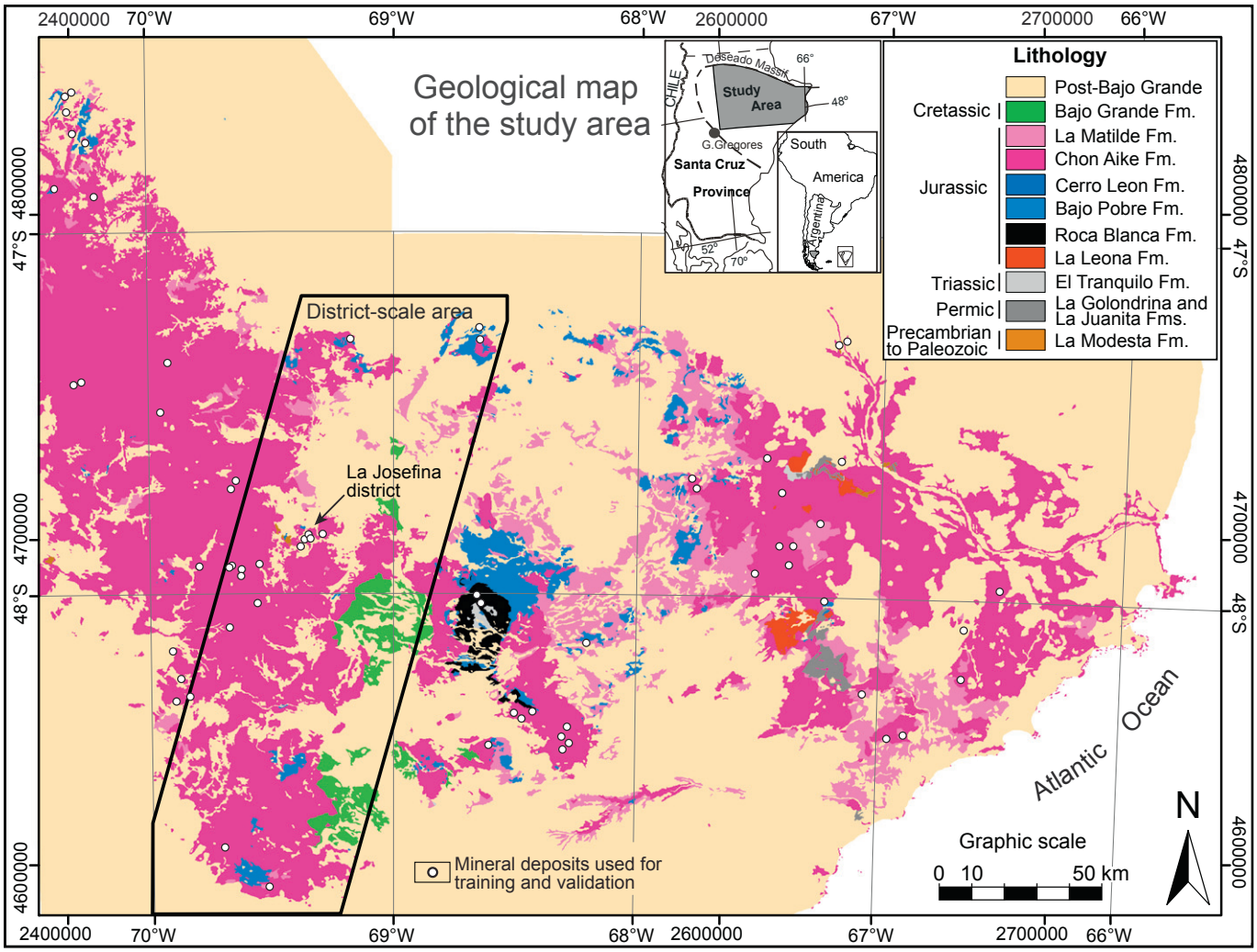

Fig. 1. Location and lithology of the study area, extracted from seven geological maps at 1:250,000 scale, published by the Argentinean Geological Mining Service.

The Chon Aike Formation is a thick sequence of rhyolitic to rhyodacitic ignimbrites, with subordinate agglomerates and volcanic breccias, and scarce tuffs and rhyolitic lava domes (Panza, 1994a). The individual ignimbrite layers are compact and usually of 5 to 15 m thick, but locally reaching 30 m. The thickness of the whole formation is difficult to determine because of upper and lower erosional boundaries (Panza, 1982), but in general it varies between 200 and 600 m (Panza, 1994a), reaching occasionally 1200 m (Sanders, 2000). The Chon Aike Formation is intercalated with the La Matilde Formation. Stratigraphic relationships between the two formations are not very well understood because of rapid lateral changes of facies and thickness of the volcanic pile (de Barrio et al., 1986).

The La Matilde Formation includes mainly tuffs and volcaniclastic–sedimentary rocks with intercalations of thin ignimbrite layers (Panza, 1994a). The tuffs are dominant, generally fine-grained or slightly sandy, either glassy or crystalline, and usually compact. The thickness of this formation is also difficult to determine, but Panza (1994a) inferred a maximum thickness of 150 m for part of the region. This formation represents a continental fluvial and partly lagoon environment contemporaneous with intense volcanic activity in distal areas.

During the last part of the Jurassic (Kimmeridgian–Tithonian) and the Cretaceous, continental sediments of the Bajo Grande and Baqueró Formations were deposited. The Bajo Grande Formation of Upper Jurassic to Lower Cretaceous age is a continental sequence lying unconformably over the Chon Aike Formation (de Barrio et al., 1986); its thickness is variable between 80 and 350 m (Panza and Marín, 1998). The Baqueró Formation of lower Cretaceous age lies on an angular unconformity over the Bajo Grande Formation. It has a thickness of 100–140 m and is composed of conglomerates, sandstones, siltstones, and shales in its lower member, and a sequence of rhythmically intercalated cinerites and tuffs in its upper member (Panza and Marín, 1998).

The Cretaceous rocks of the Bajo Grande and Baqueró Formations were partially covered by Upper Cretaceous basalts and the Sarmiento Formation (Feruglio, 1949). Later, subaqueous sediments of the Patagonia Formation (Upper Oligocene) followed by continental sediments of the Santa Cruz Formation (Miocene) were deposited. Finally, large Mio-Pliocene basaltic lava flows covered the older lithologies.

2.2. Structural geology and geodynamic setting of the Deseado Massif

The Deseado Massif is structurally characterized by rigid blocks that were deformed into gentle folds with limbs dipping less than 20° (Fernández et al., 1996). Several tectonic events produced a series of grabens, half-grabens, and horsts, which are slightly tilted to the east and have a complex internal structure with transverse faults (Ramos, 2002b). There are several fault systems in different sectors of the Deseado Massif, but the most widely observed ones (Table 1) are the El Tranquilo, Bajo Grande (Panza, 1982), La Frisia, and Zanjón del Pescado systems (Reimer et al., 1996).

Table 1
Characteristics of the four most widely observed faults systems in the Deseado Massif (extracted from Panza, 1982, 1994a; Reimer et al., 1996).

System	Movement/azimuth	
	Principal direction	Conjugated direction
El Tranquilo	sinistral / 143°–160°	dextral / 57°–65°
Bajo Grande	sinistral / 116°–130°	dextral / 21°–36°
La Frisia	dextral / 170°	sinistral / 40°
Zanjón del Pescado	sinistral / 15°	dextral / 145°

The tectonic events affecting the area during the Paleozoic included a Cambrian to Devonian compressional to transpressional deformation (Deseado orogen) along NNW trending fractures (Giacosa et al., 2010). During the Permian to Triassic, there was extensional brittle deformation along NNW fractures, which produced the La Golondrina rift. This period includes the emplacement of the La Golondrina, El Tranquilo and La Leona Formations.

The evolution of the Deseado Massif during the Mesozoic is closely related to the breakup of Gondwana and the opening of the South Atlantic Ocean (Reimer et al., 1996; Ramos, 2002b). However, some details of its geodynamic evolution are still not clear. During the Jurassic, the western margin of southern South America was a subducting margin (Gust et al., 1985; Nelson et al., 1980), while the backarc area was undergoing extension. Contemporaneous with this tectonism a widespread bimodal volcanism occurred, which included the deposition of the Roca Blanca, Bajo Pobre, Chon Aike and La Matilde Formations.

According to some authors (Echavarría et al., 2005; Uliana et al., 1985), the Jurassic extension produced large, NNW-trending half-grabens, bounded by steeply dipping normal faults, most of which were reactivated structures of the former Permo-Triassic rift (Gust et al., 1985; Echavarría et al., 2005). According to Giacosa et al. (2010) however, the most relevant structures produced by the Jurassic rifting were large WNW transtensional faults that crosscut and interacted with pre-existing NNW Paleozoic orogenic structures. The general extension would have also produced NNE structures, and purely extensive NW-oriented faults.

During the Cretaceous, SW–NE compression produced tectonic inversion and reactivation of WNW and NW normal faults, as well as thrusting, wrenching, intense folding, and formation of NW (or NNW) trending anticlines (Giacosa et al., 2010). During the Cenozoic, general E–W compression of the Andean orogeny produced tectonic inversion again, reactivating mainly pre-existing N to NNE normal faults, and uplifting a series of narrow and sub-meridional ranges, one of which divides the entire Deseado Massif into two structural domains (Giacosa et al., 2010; Japas et al., 2013). The eastern domain shows well-preserved WNW Jurassic and Cretaceous structures; while the western domain, more influenced by the Andean deformation, shows strong NNW trends, probably influenced by the inherited Paleozoic fabric (Giacosa et al., 2010). The predominance of different directions of fracturing in different sectors of the Deseado Massif may have been the result of differential tectonic rotations (Japas et al., 2013) that were observed in the area, and may have occurred in the Jurassic or early Cretaceous (Somoza et al., 2008).

2.3. Epithermal gold mineralization in the Deseado Massif

Most Au–Ag deposits in the Deseado Massif are of the low-sulfidation epithermal style (Schalamuk et al., 1997, 2002). They are characterized by multi-episodic quartz veins, and partly by stockworks, breccias and disseminations. The ore is composed of native gold, electrum, native silver, argentite, and variable amounts of pyrargirite, freibergite, petzite and other sulfosalts. Occasionally, precious metals are associated with sulfides such as galena, sphalerite, and chalcopyrite. The gangues consist mainly of different varieties of silica, together with pyrite, arsenopyrite, calcite, barite, adularia, rhodochrosite, siderite, and rare monazite. As in other low-sulfidation epithermal deposits, boiling has often been considered the main cause of Au precipitation in the Deseado Massif (Echavarría, 2004; Echavarría et al., 2005; Moreira, 2005; Rios et al., 2000). The ore-minerals in these deposits precipitated in the temperature range 150–300 °C (Fernández et al., 2008), which is consistent with temperature of formation of other epithermal deposits (Simmons et al., 2005). Interpretation of stable isotopic data of several deposits (Echavarría, 2004; Guido, 2002, 2004; Moreira, 2005) together with salinity estimates of fluid inclusions, suggested that the epithermal fluids were mixtures of magmatic and meteoric fluids (Fernández et al., 2008).

Several deposits in the Deseado Massif show evidence of an intermediate-sulfidation state of the mineralizing environment (Andrada de Palomera et al., 2012; González Guillot et al., 2004; Guido et al., 2005; Jovic et al., 2004; Dietrich et al., 2012; Moreira et al., 2004). Although low-sulfidation (LS) and intermediate-sulfidation (IS) epithermal deposits are relatively similar, they show also some differences (Einaudi et al., 2003; Hedenquist et al., 2000; John, 2001; Sillitoe and Hedenquist, 2003). Similarities are in the shape of the deposit and the way of emplacement, that involve the formation of veins and veinlets. Other similarities are in the types of gangue minerals, and style of alteration, that include the formation of illite, smectites, white micas and propylitic mineral assemblages. The main differences between the two types of deposits are: a) FeS content (mol.%) of sphalerite: 1–20 for IS and 20–40 for LS deposits; b) salinity (wt.% NaCl eq.) in fluid inclusions: <1 in LS deposits and > ~3 in IS deposits; c) abundance of sulfides, typically < 1–2 vol.% in LS and > 5 vol.% in IS deposits; d) sulfide assemblages, including increased abundances of tetrahedrite–tennantite in IS deposits; and e) higher amounts of base metals, Ag, Mn and Ba in IS deposits, and higher amounts of Au, As and Hg in LS deposits. Characteristic features of IS state of mineralizing environment were observed in several deposits in the Deseado Massif. Two of these have been classified as intermediate-sulfidation epithermal deposits (i.e., Martha and San José).

The dominant styles of hydrothermal alteration related to LISEDs in the Deseado Massif are silicification and argillic alteration. Silicification is the most conspicuous type of alteration since it results in features that are resistant to erosion that can easily be recognized in the field. These features form excellent exploration targets for the Au–Ag deposits (Schalamuk et al., 2002). At deeper levels of the epithermal paleo-systems, silicification occurred in narrow zones around epithermal fluid pathways (Andrada de Palomera et al., 2012). At surface levels, silicification resulted in the formation of wider blanket-shape silica-rich zones. In addition, silica sinters were formed at the surface at, for instance, Manantial Espejo, La Josefina, and El Macanudo (Schalamuk et al., 1997). Argillic alteration halos, consisting of illite, illite-smectite, and kaolinite formed around the narrow silicified zones that were associated with veins. The argillic alteration may grade outwards to propylitic alteration halos (Dietrich et al., 2012; Mykietiuk et al., 2005). Propylitic alteration can be formed by hydrothermal alteration but it can also be the product of earlier deuteric alteration that is unrelated to the formation of epithermal systems (Hedenquist et al., 2000). In the upper parts of the epithermal paleo-systems, the silicified zones are often associated with kaolinite-rich blankets (Rolando and Fernández, 1996; Mykietiuk et al., 2005), which may have been produced by precipitation from steam-heated waters near the paleo-water table (Fernández et al., 2008). Supergene minerals such as limonite, manganese oxides, and scarce alunite and gypsum, have also been identified and may reflect exposure of sulfide-bearing rocks to weathering processes.

The epithermal deposits in the Deseado Massif formed in a backarc rift setting (Echavarría et al., 2005) and are temporally associated with Jurassic bimodal volcanism (Schalamuk et al., 2002). Radiometric dating of alteration minerals indicate that the mineralization occurred during the Jurassic, and probably the upper Jurassic, as pointed out by Fernández et al. (2008). However the detailed correlations with the

age of the volcanic host rocks are arguably, because most dates were derived from K/Ar or Ar/Ar methods, which are potentially unreliable due to possible loss of argon. The age of part of the mineralization in the Huevos Verdes system (around 140 Ma) is amongst the youngest reported ages in the Deseado Massif (Dietrich et al., 2012), yet, these mineralized rocks are in the Bahía Laura Group and no other mineralization has been reported in younger Formations in the Deseado Massif. The Chon Aike Formation is the most frequently occurring host rock of LISEDs, but the Bajo Pobre Formation and occasionally the La Golondrina, La Leona, Roca Blanca, and La Matilde Formations also host some of those deposits (Schalamuk et al., 1997). Because of the temporal association of LISEDs with Jurassic volcanism, and the seemingly lack of mineralization in the Bajo Grande and younger Formations, we considered that those formations postdate the epithermal mineralization events and are therefore, not associated with that mineralization.

The Au–Ag deposits in the Deseado Massif are structurally controlled (Dietrich et al., 2012; Fernández et al., 2008). The epithermal vein systems were controlled by a dilatation direction consistent with the SW–NE Jurassic extension (Giacosa et al., 2010). The NNW to NW-trending faults produced the most continuous and wider veins with the highest Au–Ag grades. Locally, faults with NE–SW orientation are predominant controls on mineralization, mainly in the eastern sector of the Deseado Massif (Andrada de Palomera and Carranza, 2005); however, they produced generally thin and discontinuous mineralized veins, with low Au–Ag grades (Echavarría et al., 2005). NNE shear zones in La Josefina (Moreira et al., 2008), San Jose (Dietrich et al., 2012) and El Dorado-Monserrat (Echavarría et al., 2005), may have produced local extension and ore deposition in opening bends along general NW oriented fractures. Although many deposits are spatially associated with NE (40–60°) oriented regional faults, the faults with orientations between 140° and 170° are more efficient evidence of LISEDs occurrence than the NE-trending faults, whereas faults with orientations between 120° and 130° show weak or no spatial association with epithermal deposits (Carranza and Andrada de Palomera, 2005). This is consistent with the poor mineralization of WNW-oriented veins in districts such as San José (Dietrich et al., 2012).

In the western sector of the Deseado Massif, the mineralization was controlled along three predominant orientations: 160–170°, 140–150°, and 120–130° (Andrada de Palomera and Carranza, 2005). Orientations of 160–170° likely represent regional-scale faults limiting large blocks in the Deseado Massif (Ramos, 2002b) and are probably related to graben formation; the orientations of these faults coincide with those of the La Frisia fault system (Table 1). Orientations of 140–150° correspond with the general trends of the El Tranquilo fault system, which is related to mineralization in some deposits (e.g., the La Josefina deposit; Moreira et al., 2008). Orientations of 120–130° correspond with directions of the Bajo Grande faults system.

3. Methods

The WofE method was used to map prospectivity for LISED in the Deseado Massif (Fig. 1), using two different geological datasets. One dataset is relatively general, and was produced from available data easy to combine for the whole study area. This dataset is hereafter called the regional-scale dataset, while the whole study area is called the regional-scale area (70,828 km^2), which includes most of the Deseado Massif. The other dataset, hereafter called the district-scale dataset, contains more detail, and the area it covers is called the district-scale area (11,947 km^2); it was derived from data that are more tedious to process and more difficult to combine appropriately for the whole regional-scale area. Regional-scale and district-scale models were produced from the WofE analysis of the regional- and district-scale datasets, respectively. These two models were selected amongst six models produced by using different combinations of data layers with the aim of obtaining statistically robust models, and were tested by means of conditional independence (CI) tests.

The LISED prospectivity was mapped based upon the locations of 65 LISEDs and lithological, structural, and alteration evidence. These features were represented in raster maps, with 1000 m and 100 m spatial resolutions in the regional-and district-scale areas, respectively. The locations of known LISEDs were digitized from mining cadastral maps, published maps, and data known by the authors. The relevance of each geological evidence layer was assessed by WofE modelling.

The WofE calculations and CI tests were carried out using the Spatial Data Modeller (SDM) (http://www.ige.unicamp.br/sdm/default_e.htm) module for the ArcGIS software (Sawatzky et al., 2009).

3.1. Weights-of-evidence method

Weights-of-evidence is a quantitative data-driven method that uses a log-linear form of the Bayesian probability model (Bonham-Carter, 1994). In mineral prospectivity mapping, this method can estimate the relative importance of individual layers of evidence by statistical means, minimizing subjective bias in quantifying spatial associations between every layer of evidence and mineral deposits used for training. It allows the user to calculate weights for different classes in every evidential layer, and to produce a probability map of the occurrence of the type of deposits used for training. This can be done even using a limited number of mineral deposits (Carranza, 2004).

Given a study area, T, composed of a number of area units N[T] (unit cells in a raster map) containing a number of deposits N[D] and assuming that each deposit occupies one cell, the *prior probability* that a randomly selected cell in the map contains a deposit, when no other information is available, can be estimated as P[D] = N[D] / N[T]. If evidence B (represented by a binary map) is present, the probability of finding a new deposit can be expressed as a *conditional (or posterior) probability* (P[D|B]). The algorithms used as basis of the WofE calculations can be found in Agterberg and Cheng (2002), Bonham-Carter (1994), Carranza (2004), and Carranza and Hale (2000).

In WofE modelling, updating of posterior probabilities by the use of two or more evidence maps (B1 and B2), is only possible if those maps are approximately conditionally independent of each other with respect to the pattern of mineral deposits (D) (Agterberg and Cheng, 2002). The assumption of CI can be verified with two tests.

A pairwise test between binary maps B1 and B2 can be executed before combining the maps. If B1 and B2 are conditionally independent, then, in their overlap region the number of predicted D should be equal to the number of observed D. The possible overlap conditions of observed and predicted deposits with B1 and B2 can be represented in a 2 × 2 contingency table, and the divergence between numbers of observed and predicted D can be calculated with the chi-square (X^2) statistic (Moor and McCabe, 1999). Values of X^2 above 3.84, which is the critical value with one degree of freedom at the 95% significance level (Davis, 1986), indicate that the assumption of CI has been violated (Bonham-Carter, 1994). Frequencies in each cell of the contingency table should be at least 5 (Carranza, 2004; Snedecor and Cochran, 1967); therefore, the X^2 test of CI was only applicable to the final regional-scale predictive model.

After all evidence maps are combined, the "new omnibus test" (NOT) (Agterberg and Cheng, 2002) of CI can be used to test whether the difference between the number of predicted D ($N\{D\}_{pred}$) and that of observed D (N{D}) is significantly greater than. The NOT is a one-tailed test of the null hypothesis that $N\{D\}_{pred} - N\{D\} = 0$; being $(N\{D\}_{pred} - N\{D\}) / \sigma N\{D\}_{pred}$ the test statistic ($\sigma N\{D\}_{pred}$ = standard deviation of predicted D). Because the values of NOT are assumed to approximate a standard normal distribution, the probability that $N\{D\}_{pred} - N\{D\}$ is statistically greater than zero can be estimated (from statistical tables). A probability of 50% is expected when two layers of evidence are conditionally independent; higher probabilities indicate conditional dependence, and when they are greater than 95% or 99% the hypothesis of CI should be rejected (Agterberg and Cheng, 2002).

3.2. Preparation of evidence layers

Based on the above-described characteristics of the LISEDs in the Deseado Massif, and considering the characteristics of these types of deposits worldwide, a set of deposit recognition criteria was defined for each mapping scale (Table 2), and employed for extracting the lithological, alteration and structural evidence used as input for the WofE modelling.

3.2.1. Lithology

For prospectivity mapping, lithological units older than the Bajo Grande Formation were considered favourable for mineralization. The favourable lithologies include the La Modesta, La Golondrina, La Juanita, El Tranquilo and Roca Blanca Formations. The Bajo Grande and younger units were considered unfavourable because they are interpreted as post-epithermal mineralization.

Lithological evidence was extracted from two sources with different detail of mapping, both published by the Argentinean Geological Mining Service. One is a 1:750,000 scale geological map (Dirección Nacional del Servicio Geológico, 1994), hereafter called the "generalized lithological map". The second source is a set of seven geological maps published at a scale of 1:250,000 (Cobos and Panza, 2003; Giacosa et al., 1998; Panza, 1994a,b, 2001; Panza and Cobos, 2001; Panza and Marín, 1998), hereafter called the "detailed lithological map". Those maps were georeferenced, and the boundaries of favourable lithology (Fig. 1) were digitized on-screen. Then, the resulting maps were converted into binary raster maps of favourable lithology for LISED occurrence.

Accuracy is not indicated in any of the geological maps, but we estimated the error for the georeferenced maps by comparing the position of features in the maps (e.g., intersections of roads, small lagoons, etc.) with their position on well georeferenced Landsat images. The median of errors for 105 points observed in the detailed lithological map is 268 m, while that of 46 points observed in the generalized lithological map is 1249 m. Most of these errors are likely products of the original mapping process, but scanning and georreferencing may have also contributed to them.

3.2.2. Hydrothermal alteration

We considered silicic and clay alterations as good indicators of LISEDs, and mapped them with remote sensing data, after testing several techniques of image processing and comparing the results with ground control areas located in the La Josefina district (Fig. 1). These areas contained indications of kaolinite alteration, argillic alteration (smectite and illite), and silicic rocks (silicified rocks, silica sinter and opaline bodies).

At regional-scale, the band ratio 5/7 of 11 Landsat 7 ETM+ scenes was used to map clay alteration. The scenes were acquired in different years, seasons and times (from 1999 to 2002 and from September to February); therefore, for minimizing the difference in illumination between scenes, a sun angle correction was applied before calculating the band ratio; this correction consisted in dividing the pixel value by the sine of the solar elevation (Prakash, 2001). The band ratio 5/7, which takes advantage of strong absorption in band 7 (Sabins, 1999) due to clays (Fig. 2), was preferred to the Crósta technique using bands 1, 4, 5 and 7 (Crósta and Moore, 1989), because the former better indicates areas of alteration in the La Josefina deposit and it is simpler to calculate and interpret. After the band ratio was calculated a low pass 9×9 kernel filter was applied to minimize the pepper-salt effect. Areas with band 5/7 ratio values larger than 1.18 (threshold based on ground control in the La Josefina deposit) were considered altered. Unfortunately, several lagoons and small wet valleys were identified as altered areas, presumably because of clays deposited from water. Because water has a strong absorption in band 5, a mask of DN-pixel values below 70 in band 5 (empirically determined) was applied to eliminate false anomalies, finally resulting in a binary regional clay alteration evidence map.

At district-scale, four on-demand ASTER L2 scenes (Abrams et al., 2002) were used to map clays with short-wave infrared (SWIR) bands, and silica with thermal infrared (TIR) bands. The SWIR bands consist of surface reflectance, calculated by NASA after applying atmospheric corrections on ASTER Level-1B data; while the TIR bands consist of surface emissivity, obtained by separating emissivity from temperature. The four scenes were acquired at around 14:25 of the 2nd of March of 2002.

After comparing with the *spectral angle mapper* classifier, the Crósta technique, and other band ratios methods, the ASTER band ratio 4/6 was selected to map clay alterations, for it enhances better the known areas of alteration in the La Josefina deposit, and it is simpler to generate and interpret. This ratio, already used by Carranza et al. (2008), is aimed to detect illite, montmorillonite, and kaolinite (Fig. 2), which are abundant in LISEDs. The 4/6 band ratio image was then filtered with a 5×5 kernel low pass filter to minimize the pepper-salt effect.

The silica abundance was represented by the K_{silica} index (Miyatake, 2002; MMAJ, 2000), calculated as $K_{silica} = \log((E[10] + E[11] + E[12]) / 3 / E[13]) * (-1)$, where E[n] are values in each ASTER TIR band n. Prior to calculating this index, a 3×3 kernel averaging filter was applied to reduce the effect of striping. The resultant image shows anomalously

Table 2
Recognition criteria for epithermal deposits in the Deseado Massif at regional- and district-scale, concepts used to define the criteria and sources from which the evidence layers were derived.

	General concepts used to define the deposit recognition criteria	Deposit recognition criteria (RC) and sources of evidence	
		Regional-scale	District-scale
Lithology	Only rocks contemporaneous or older than the epithermal mineralizing events are mineralized. Bajo Grande and younger Formations were not recognized as hosts of epithermal deposits in the Deseado Massif.	RC: outcropping rocks older than the Bajo Grande Formation. Evidence extracted from a generalized lithological map	RC: outcropping rocks older than the Bajo Grande Formation. Evidence extracted from a detailed lithological map. Used to restrict the area to analyse with WofE.
Alteration	The epithermal paleo-systems deposited silica and some kaolinite in veins; silicification is immediately around veins; illite and smectite surrounding the silicification; and chlorite-rich propylitic alterations surrounding laterally and below the other alterations, and may occasionally be unrelated to the epithermal system (deuteric). Silica and kaolinite were also deposited in the upper parts of paleo-systems above the zone of fluid boiling.	RC: abundance of kaolinite, illite, smectite and probably chlorite. Evidence extracted from Landsat (band ratio 5/7).	RC: abundance of kaolinite, illite, and smectite. Evidence extracted from ASTER (band ratio 4/6). RC: abundance of silica. Evidence extracted from ASTER (K_{silica} index).
Structures	Regional-scale structural zones with orientations from NW–SE quadrants were produced or reactivated by general SW–NE extension at the time of mineralization, and therefore, some of them likely acted as the main conduits for ascendant paleo-fluids. Locally, rock permeability is an important control for fluid flow and mineral deposition.	RC: proximity to 140–170° oriented fracture zones. Evidence extracted from different remote sensing products (lineaments digitized at 1:1,500,000 or smaller displayed scale).	RC: overall rock permeability Evidence extracted from different remote sensing datasets (density of lineaments digitized at displayed scale ~1:100,000).

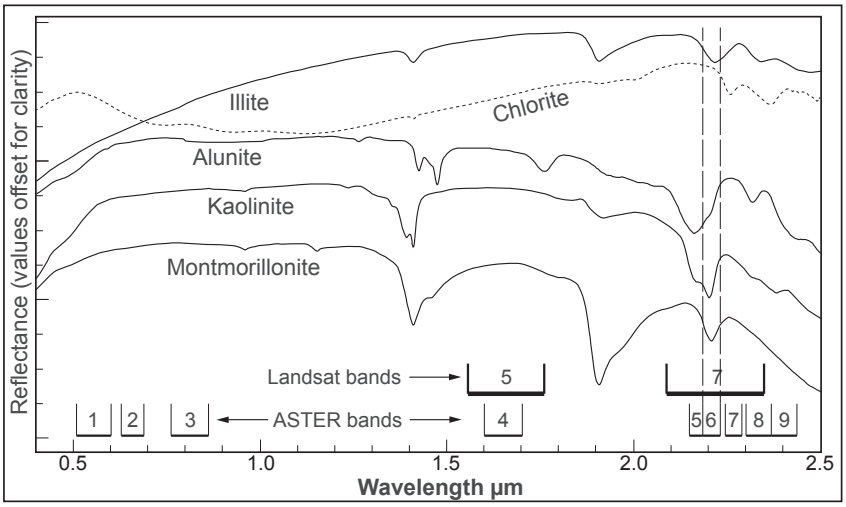

Fig. 2. Spectra of four common alteration minerals (Grove et al., 1992 — JPL1 data) and their relationships with ASTER and Landsat 7 ETM+ data.

high values, coincident with siliceous outcrops. An image of band ratio 13/12 showed similar results but the image of the K_{silica} index showed better definition of siliceous outcrops.

The district-scale alteration data from the studied areas were classified based on percentiles of 4/6 band ratios and K_{silica} index, producing evidence maps for the spatial analysis at the district scale.

3.2.3. Structures

In epithermal systems, areas of structural weakness can act as pathways of hydrothermal fluids, and localize mineralization. However, structural controls on mineralization may be scale-dependant, and therefore, while structural zones should be distinguished for regional-scale exploration (White and Hedenquist, 1990), they may not be useful for target generation at larger scales (Austin and Blenkinsop, 2009), where local controls (even small fractures) should be considered because they modify rock permeability and may control the location of deposits.

In this study, regional structural controls, predominant in the western sector of the Deseado Massif, were considered representative for the whole area of study because they are the most persistent structural controls throughout the entire region (Andrada de Palomera and Carranza, 2005). Regional structural features trending 140–150° and 160–170° were combined and referred to as NW to NNW trending structural controls (140–170°). Regional structural features with orientations of 120–130° were not used because they show weak or no spatial association with LISEDs (Carranza and Andrada de Palomera, 2005).

Regional-scale fault zones with orientations of 140–170° were inferred from lineaments digitized on-screen at a scale of 1:1,500,000 or smaller, mainly on Landsat and 90 m resolution shaded-relief images, derived from Shuttle Radar Topography Mission data. To enhance lineaments with different orientations, several directions of illumination were applied as done by Asadi (2000) and Carranza (2002). Inferred fault zones were represented by linear patterns of 2000 m width, which were buffered outwards in steps of 2000 m, up to 20,000 m, producing a map of proximity to regional-scale structures.

Lineaments for the district-scale modelling were digitized on images displayed on-screen at a scale of around 1:100,000. Following Carranza (2002), Dinger et al. (2002), Koike et al. (1995), Hung et al. (2005) and Lepage et al. (2000), we considered most lineaments as representative of fractures (either faults or joints). Landsat R-G-B colour composite 7-4-1 were the mostly used images, but combinations of the 7-4-1 composite with shaded-relief images, and edge-enhanced band 7 images, were also used. Density of lineaments (total length of lineaments per pixel area) was calculated for an output resolution of 2000 m; the pixel size of the lineament density image was then reduced to 500 m, and the image resampled to 100 m resolution. Finally, density values were classified using percentiles of lineament density, and prepared as an evidence map.

3.3. Spatial association analysis and predictive mapping

The spatial associations of LISEDs with lithology, hydrothermal alteration, and structures were investigated using positive and negative weights (W^+ and W^-), the contrast (C), and the studentized contrast (SigC), derived from the WofE calculations. These spatial association parameters were calculated for patterns in six evidence maps, including the binary patterns of lithological and clay alteration regional maps, the cumulative classes in the map of proximity to regional structures, and the cumulative classes in the evidence maps of clay alteration (band ratio 4/6), silica (Ksilica index), and density of lineaments.

Each of the six mentioned evidence maps were generalized to a binary map with one class (predictor pattern present) carrying the value of W^+, and the other (predictor pattern absent) carrying the value of W^-. For each multiclass evidence map, a cumulative class with optimum spatial association with LISEDs was defined as that with the highest *C*, being $SigC \geq 2$, and was used as threshold for the generalization. The predictor pattern present includes from the percentile class 90–100 to the class with optimum spatial association; the predictor pattern absent includes the remaining cumulative classes. For the regional evidence maps of lithology and clay alteration, no generalization was necessary. The binary maps were then used for the pairwise CI test described earlier.

These binary predictor maps can also be used to calculate the posterior probability maps, but the SDM software does this directly from the weights tables, as well as carrying out the NOT test for conditional independence, without the need of generating binary maps. The posterior probability maps were later re-classified into binary favourability maps; posterior probabilities higher than the prior probability were considered favourable to explore for LISEDs, while those lower than the prior probability were considered unfavourable.

3.4. Assessment of predictions at regional- and district-scales

Seven indicators were used to evaluate the effectiveness and usefulness of mapping at the district and regional scales: *success rate*, *prediction rate*, weights, *C*, *SigC*, NOT test of CI, and percentage of area reduction when determining favourable areas.

The *success rate* was based on the total number of deposits N[D], for training as well as validating, and calculated as the percentage of N[D] located in favourable areas of the favourability map, and considered

indicative of the goodness of fit and overall efficiency of the model's predictions. The *prediction rate* was based on the leave-one-out cross validation (LOOCV) method, and calculated using the procedure of spatial association analysis and posterior probability and favourability maps calculation that was repeated N[D] times, selecting a different training set of N[D] − 1 deposits every time; the resulting favourability map was validated with the single deposit left out. Then, the *prediction rate* is defined as the percentage of the N[D] instances with the validation deposit located in favourable cells, and also considered as indicative of the efficacy of the predictive models and favourability maps.

Then, we compared the predictions inside the district-scale area based on the regional- and district-scale models. This allowed us to evaluate the effectiveness and usefulness of each model.

4. Results

4.1. CI tests of the different models

The results of testing the CI for six different contrasting models are shown in Table 3. For regional-scale mapping, using the generalized lithological map and the alteration and regional structural evidence layers (model Reg-1), the results from NOT are sufficient to accept the assumption of CI, although they indicate that there is considerable conditional dependence between layers. In addition, values from the X^2 test of CI for the pair of structural and lithological evidence layers (3.53) is very close to the 3.84 critical value, suggesting relatively high conditional dependence between these two layers. The structural-alteration and alteration-lithology pairs show low X^2 values.

By using the detailed lithological map and the alteration and regional structural evidence layers (model Reg-2), the results from NOT are less satisfactory than with the previous dataset. Results from NOT indicate that the hypothesis of CI could still be accepted, but the "CI ratio" (simple ratio N{D} / $N\{D\}_{pred}$), is below 0.85, which may indicate a CI problem (Bonham-Carter, 1994).

Because models Reg-1 and Reg-2 show relatively high conditional dependence, probably resulting from pairs that include lithology, two other models (Reg-3 and Reg-4) were produced based on restricting the area for WofE calculations to only the favourable lithology, and carrying out the predictions using the alteration and structural evidence layers. Restricting the area to the favourable lithology of the generalized lithological map (model Reg-3), only 51 training deposits were used. The remaining 14 deposits are in areas mapped as unfavourable lithology; although it is known that most of them are in reality hosted by favourable lithological units, reflecting the effects of low accuracy of the generalized lithological map. Restricting the area to the favourable lithology of the detailed lithological map (model Reg-4), allows using most of the original training deposits, reflecting the higher accuracy of the detailed lithological map in contrast to the generalized lithological map. For both of these models (Reg-3 and Reg-4), values from NOT decreased below 50%, the value of the NOT statistic is negative, and the CI ratio is above 1, because the number of predicted deposits is lower than the number of training deposits. This may have resulted from a decrease of spatial association noticed for the structural evidence when using Reg-3 and Reg-4, probably as a consequence of omitting some deposits; and because of decreasing the number of predictor maps, with potentially negative effects (Harris and Sanborn-Barrie, 2006), although with the positive effect of decreasing the conditional dependence, which agrees with the idea of Agterberg and Cheng (2002) that CI decreases as additional map layers are included.

For district-scale mapping, two models (Dist-1 and Dist-2) were tested. Model Dist-1 (Table 3) included 18 training deposits, located in the district-scale area, and four evidence layers: clay alteration (ratio 4/6), silica abundance (K_{silica} index), detailed lithology and density of lineaments. The results from the CI test were not satisfactory; the NOT-probability is relatively high and the CI ratio is too low, showing that there is relatively high conditional dependence. Model Dist-2 was produced only with data restricted to areas of favourable lithology of the detailed lithological map. Evidence layers of clay alteration (ratio 4/6), silica abundance (K_{silica} index) and density of lineaments, as well as the 17 deposits located in the restricted area, were used in this model. The CI tests for this dataset improved significantly, with the CI ratio and NOT probability very close to the optimum values for a conditionally independent dataset.

Finally, model Reg-1 was selected as the most suitable for regional-scale predictions, because it is statistically robust, and it uses for the WofE calculations in the whole study area all the training deposits and all three evidence layers. Model Dist-2 was selected as the most suitable prospectivity model for district-scale predictions, because it yields satisfactory results from the CI tests, and the number of training deposits remained almost the same after the lithological restriction.

4.2. Spatial association analysis and predictive mapping in the regional-scale area

The results of the spatial association analysis (Table 4) show that the highest and most reliable values of contrast (highest *C* and *SigC*) are for the lithological evidence (Fig. 3a), while the lowest are for the clay alteration evidence (Fig. 3b). The cumulative class 10,000–12,000 m from

Table 3
Results of the tests of conditional independence produced from six models.

Model	Study area	Predictor evidence layers	No of deposits	CI ratio	NOT statistic	NOT probability	Remarks
Reg-1	Complete regional-scale area	3 layers: generalized lithology, clay alteration, structures	65	0.89	0.6588	74.50%	Sufficient to pass the tests. The X^2 test shows conditional dependence between structural and lithological evidence layers.
Reg-2	Complete regional-scale area	3 layers: detailed lithology, clay alteration, structures	65	0.84	0.9228	82.20%	NOT probability is sufficient to pass but CI ratio indicates a problem.
Reg-3	Favourable lithologies of generalized lithological map in the regional-scale area	2 layers: clay alteration, structures	51	1.03	−0.1516	44.00%	NOT probability < 50%, CI ratio > 1 and negative values for NOT statistic may indicate problems. Area restriction decreased the number of deposits because of low map accuracy.
Reg-4	Favourable lithologies of detailed lithological map in the regional-scale area	2 layers: clay alteration, structures	60	1.02	−0.1327	44.70%	NOT probability < 50%, CI ratio > 1 and negative values for NOT statistic may indicate problems.
Dist-1	Complete district-scale area	4 layers: detailed lithology, clay alteration, silica alteration, structures	18	0.46	1.1099	86.60%	Relatively high conditional dependence.
Dist-2	Favourable lithologies of detailed lithological map in the district-scale area	3 layers: clay alteration, silica alteration, structures	17	0.99	0.0288	51.10%	Results of CI tests improved by restricting the study area to favourable lithology.

Table 4
Results from the spatial association analysis between regional-scale evidence and LISEDs, including weights (W), contrasts (C), and studentized contrast (SigC). Favourable lithology includes the Chon Aike, La Matilde and Bajo Pobre Formations. Underlined classes show optimum spatial association with LISEDs, and were considered as predictor patterns.

	Binary and cumulative evidence classes	Cumulative pixels in evidence class	Cumulative deposits in evidence class	W^+	W^-	C	SigC
	Favourable lithology	25,917	51	0.7640	−1.0804	1.8442	6.1102
	Clay alteration	25,144	43	0.6232	−0.6453	1.2685	4.8372
Structures — 140–170°	0 m	2312	8	1.3297	−0.0982	1.4280	3.7763
	0–2000 m	7168	23	1.2540	−0.3303	1.5843	6.1006
	2000–4000 m	12,148	31	1.0243	−0.4602	1.4845	5.9732
	4000–6000 m	17,009	38	0.8910	−0.6043	1.4954	5.9374
	6000–8000 m	21,805	44	0.7890	−0.7624	1.5514	5.8466
	8000–10,000 m	26,379	49	0.7061	−0.9364	1.6425	5.7023
	10,000–12,000 m	30,582	53	0.6366	−1.1249	1.7614	5.5082
	12,000–14,000 m	34,446	53	0.5174	−1.0239	1.5413	4.8198
	14,000–16,000 m	38,022	55	0.4556	−1.1028	1.5583	4.5319
	16,000–18,000 m	41,317	57	0.4081	−1.2201	1.6282	4.3117
	18,000–20,000 m	43,902	57	0.3473	−1.1284	1.4757	3.9079
	>20,000	70,828	65	0.0002	6.9927	−6.9929	−0.4945

regional-scale structures shows optimum spatial association with LISEDs, including high number of deposits and showing high *C* and *SigC* (Table 4). Therefore, the 12,000 m distance around structures became the external border of the predictor pattern present, in the regional-scale predictor map (Fig. 3c). The predictor maps (Figs. 3a, b, c) represent results from the spatial association analysis (Table 4) that can be used for the generation of the posterior probability map and for the tests of CI.

The pairwise test of CI for the regional-scale binary predictor maps (Figs. 3a, b, c) shows values of X^2 below the critical value of 3.84 (Fig. 3d), suggesting that the assumption of CI is valid, and that the predictor maps can be used for the regional-scale prediction of LISEDs occurrence. This prediction is represented by the regional-scale posterior probability map (Fig. 4), which includes eight discrete values of posterior probability, and predicts a total of 73 deposits, which is 12% more than the observed number of deposits.

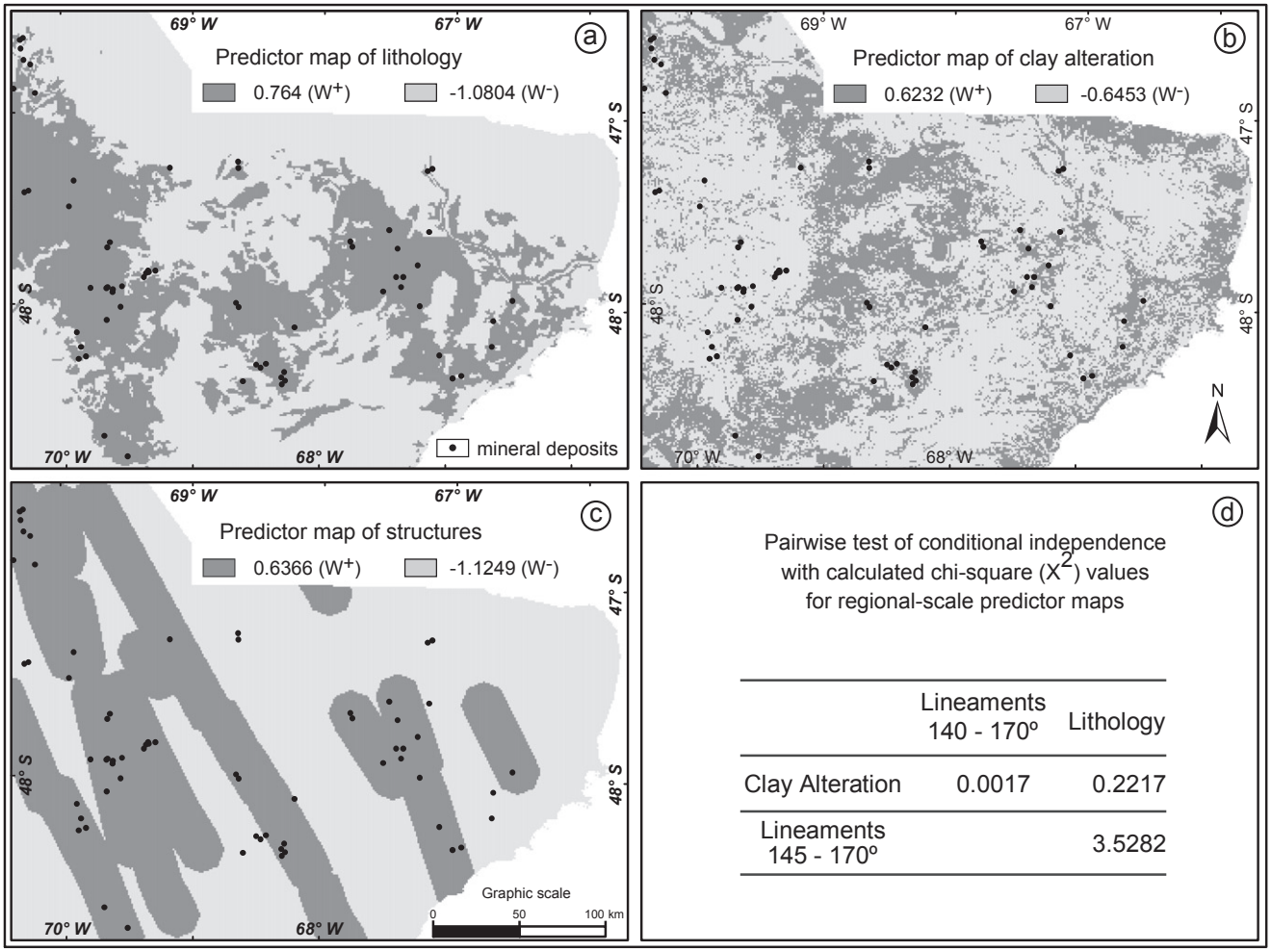

Fig. 3. a), b), c) Binary predictor maps representing results from the spatial association analysis (Table 5) of the regional-scale dataset corresponding to model Reg-1 (Table 4). These maps are useful for conditional independence tests and generating posterior probability maps. d) Results of pairwise test of conditional independence for the predictor maps.

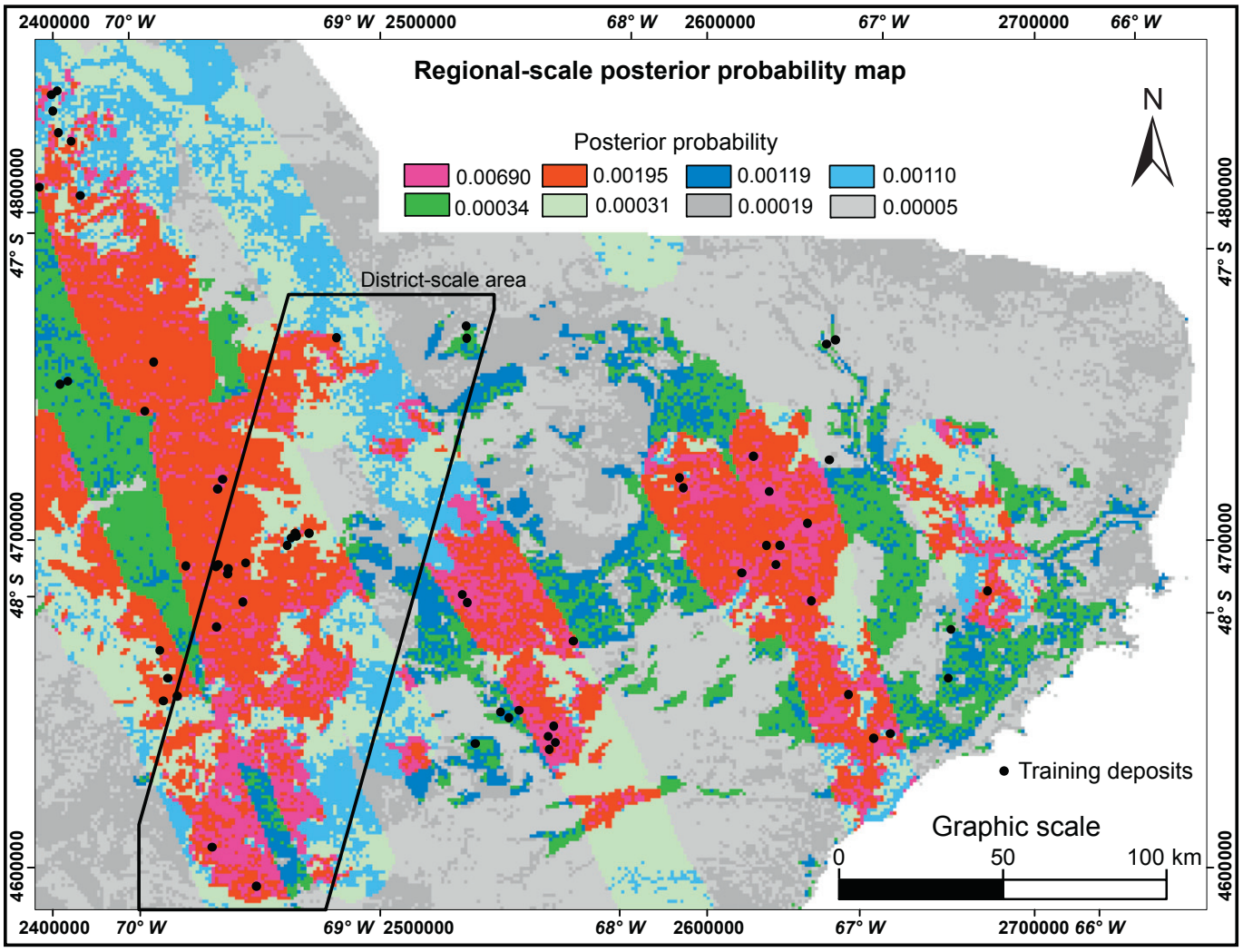

Fig. 4. Regional-scale posterior probability map. Classes of posterior probability are discrete values produced directly from the WofE calculations.

Posterior probabilities higher than the prior probability, which is 0.000918, were considered favourable for LISEDs occurrence, while those lower than the prior probability were considered unfavourable, obtaining the favourability map in Fig. 5. This favourability map shows that about 35% of the regional-scale area is favourable for LISEDs discovery. The favourable area contains 54 of the 65 deposits used for training; therefore, the regional scale predictive model has about 83% success rate. In addition, 54 out of 65 of the predictions resultant from the LOOCV method, predicted as favourable the cells corresponding to validation deposits; therefore, the "Prediction Rate" is equal to the "Success Rate" (83%).

4.3. Spatial association analysis and predictive mapping in the district-scale area

The district-scale prospectivity mapping was carried out with the district-scale dataset restricted to the areas of favourable lithology of the detailed lithological map (model Dist-2 in Table 3). This restricted area includes 17 training deposits and 5260.54 km^2 (526,054 cells), which is 44% of the total district-scale area. Therefore, the prior probability of LISEDs in the restricted area is 0.000032.

From the spatial association analysis of the district-scale evidence layers (Table 5), the lowest value of *C* is for the band ratio 4/6, which represents clay alteration; higher values are for the K_{silica} index, representing silica abundance, and for density of lineaments. The optimum spatial association for band ratio 4/6 occurs in the cumulative percentile class 90–100, which includes only 35% of the deposits. In contrast, the cumulative classes with optimum spatial association for density of lineaments and K_{silica} index include 88% and 94% of the deposits respectively.

Three predictor maps (Fig. 6), represent the generalization of cumulative percentile classes of evidence (Table 5) into binary maps. These maps show predictor patterns present and absent, which carry respectively the W^+ and W^- weights calculated for the classes with optimal spatial association with the training deposits.

The final results from the district-scale prospectivity mapping are a posterior probability map and a favourability map (Fig. 7a, b). The district-scale posterior probability map (Fig. 7a) shows all eight discrete classes of posterior probability produced by the WofE calculations. The district-scale favourability map (Fig. 7b), shows as favourable for LISEDs occurrence, the areas in which the posterior probability is higher than the prior probability.

Using the district-scale geological dataset, the prospective area, initially equivalent to the total district-scale area (11,946.65 km^2), was reduced to 44% (5260.54 km^2) by considering only the favourable lithologies, and it was further reduced to 12.7% of the total (1520.68 km^2) by applying WofE. This relatively small percentage of the initial area is the area that is favourable for discovery of LISEDs in the district-scale area.

Sixteen out of 17 training deposits are in areas identified as favourable for LISEDs occurrence; therefore, the success rate is 94.12%.

In addition, from the LOOCV method, 14 deposits left-out successively for validation were predicted as favourable areas in the 17 predictions; therefore, the prediction rate is 82.35%.

4.4. Assessment of regional- and district-scale predictions

The comparison of predictions by the regional- and district-scale models in the district-scale area provided an assessment of the relative effectiveness of the two models for predicting favourable areas for discovering new deposits. The regional-scale model predicted 57.1% of the district-scale area as favourable, while the district-scale model predicted as favourable only 12.7% of the same area. In addition, 3.3% of the areas predicted as unfavourable by the regional-scale dataset in the district-scale area, are predicted as favourable by the district-scale model. Considering only the area of favourable lithology of the detailed lithological map, in the district-scale area, a confusion matrix (Table 6) shows that: (a) the regional-scale model delineates 83.8% of the considered area as favourable (i.e., 100 ∗ (440,931 / 526,054), while the district-scale model delineates 28.9% of the same area as favourable (i.e., 100 ∗ (152,068 / 526,054); (b) only 30.6% of the area mapped as favourable by the regional-scale model was also mapped as favourable by the district-scale model (i.e., 100 ∗ 135,040 / 440,931); and (c) 20% of the areas predicted as unfavourable by the regional-scale model are indicated as favourable by the district-scale model (i.e., 100 ∗ 17,028 / 85,123).

5. Discussion

5.1. Prospectivity mapping for LISEDs in the Deseado Massif

The relatively high success-rate and prediction-rate of the favourability maps imply that both the regional- and district-scale predictive models are effective and useful guides for exploration of LISEDs in the Deseado Massif. However, the equal values for success-rate and prediction-rate for the regional-scale model is unexpected because, as expressed by Chung and Fabbri (2003), we assume that the predictive model is correct and therefore, the success rate should be higher than the prediction rate. This may indicate problems with the regional-scale predictive model or with the data from which the model derives. Although difficult to compare exhaustively, the success-rate (83%) for our regional-scale model, is slightly higher than the 80% obtained for the same region by Carranza and Andrada de Palomera (2005) for areas with moderate and high potential for epithermal deposits. On the other hand, our prediction rate (83%) is lower than their prediction rate (97.91%). Although this gives the impression of a better validation for the model produced by Carranza and Andrada de Palomera (2005), it is more likely that their prediction rate, noticeable higher than their success rate, indicates problems with their predictive model. These problems may have been partially solved with the regional-scale model we produced, because of the use of different methods of mapping and validation, allowing us to use more training deposits.

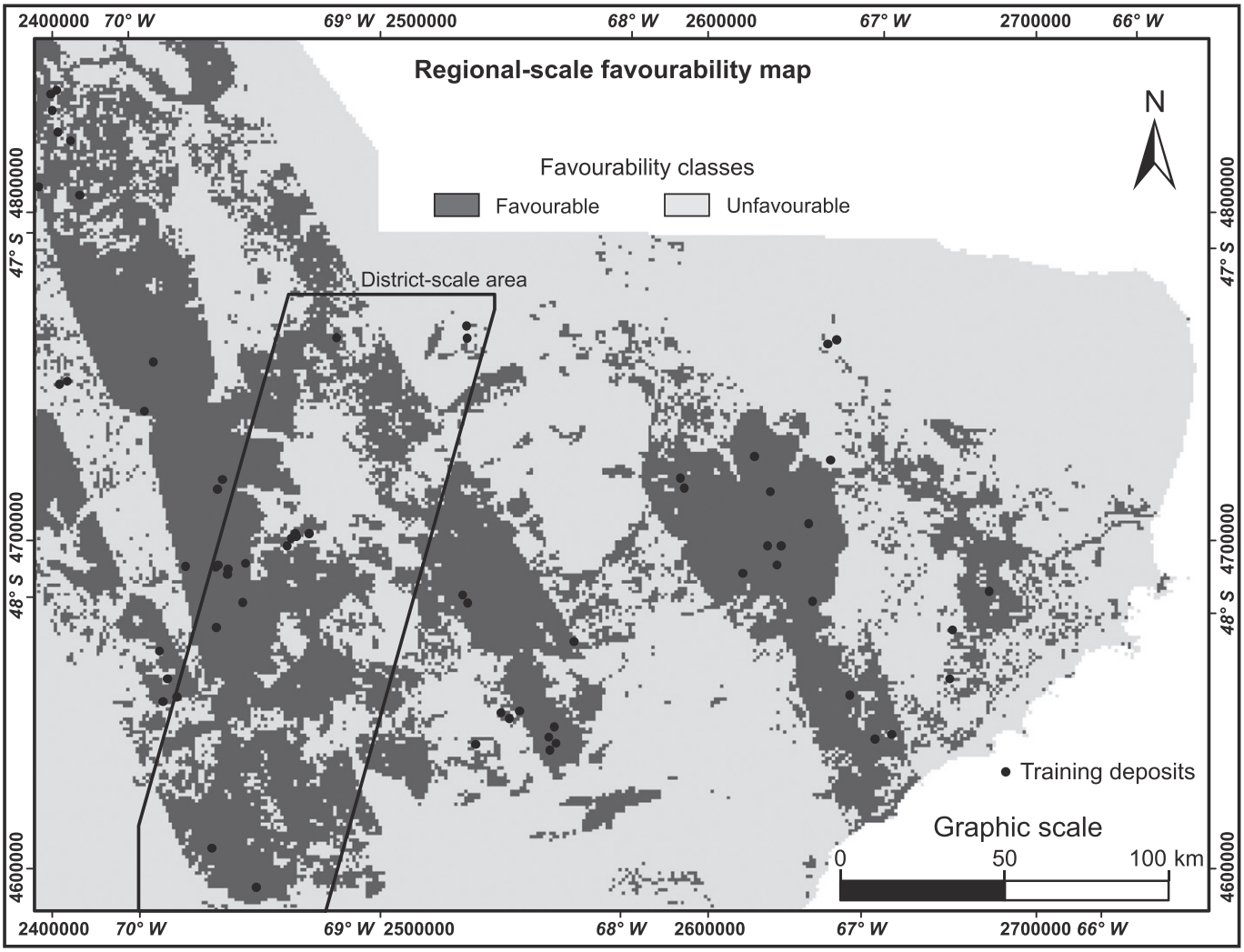

Fig. 5. Regional-scale favourability map. Favourable areas are those with posterior probabilities higher than the prior probability.

Table 5
Results from the spatial association analysis between LISEDs and district-scale evidence layers inside areas of favourable lithology of the high-resolution lithological map. The spatial association parameters include weights (W), contrast (C), and studentized contrast (SigC). Underlined classes show optimum spatial association and were considered predictor patterns.

Evidence maps	Cumulative evidence classes (percentiles)	Cumulative pixels in evidence class	Cumulative deposits in evidence class	W+	W−	C	SigC
K-index	90–100	43,382	3	0.7608	−0.1081	0.8689	1.3657
	80–90	91,928	7	0.8571	−0.3386	1.1957	2.4263
	70–80	143,040	9	0.6663	−0.4365	1.1028	2.2694
	60–70	194,299	12	0.6477	−0.7628	1.4105	2.6499
	50–60	243,551	14	0.5759	−1.1129	1.6889	2.6545
	40–50	302,387	16	0.4931	−1.9780	2.4711	2.3973
	30–40	364,670	17	0.3658	−6.2568	6.6226	0.6621
	20–30	421,846	17	0.2202	−5.8194	6.0396	0.6038
	10–20	479,139	17	0.0928	−5.0213	5.1142	0.5113
	0–10	526,054	17	−0.0006	10.3399	−10.3405	−0.7311
Band Ratio 4/6	90–100	44,909	6	1.4194	−0.3461	1.7655	3.4785
	80–90	98,637	9	1.0380	−0.5461	1.5842	3.2601
	70–80	148,994	10	0.7309	−0.5543	1.2852	2.6079
	60–70	214,013	10	0.3688	−0.3650	0.7338	1.4890
	50–60	269,569	10	0.1380	−0.1690	0.3069	0.6228
	40–50	326,392	13	0.2090	−0.4782	0.6872	1.2019
	30–40	381,592	14	0.1269	−0.4422	0.5691	0.8945
	20–30	431,552	15	0.0729	−0.4233	0.4961	0.6591
	10–20	482,235	16	0.0263	−0.3479	0.3742	0.3631
	0–10	526,054	17	−0.0006	10.3399	−10.3405	−0.7311
Density of Lineaments	90–100	52,489	4	0.8579	−0.1632	1.0211	1.7858
	80–90	105,018	10	1.0807	−0.6646	1.7453	3.5416
	70–80	157,585	14	1.0113	−1.3786	2.3899	3.7565
	60–70	210,164	15	0.7924	−1.6301	2.4225	3.2180
	50–60	262,824	15	0.5688	−1.4477	2.0165	2.6787
	40–50	315,400	16	0.4510	−1.9181	2.3690	2.2983
	30–40	368,066	17	0.3566	−6.2355	6.5921	0.6590
	20–30	420,741	17	0.2228	−5.8299	6.0528	0.6051
	10–20	473,388	17	0.1049	−5.137	5.2419	0.5240
	0–10	526,054	17	−0.0006	10.3399	−10.3405	−0.7311
	Total pixels = 526,054 Total pixels with deposits = 17						

Results of CI tests obtained by using different layers of evidence in various combinations for prospectivity mapping, show that the lithological evidence layers produce relatively high conditional dependence with other layers (mainly structural evidence), regardless of the accuracy of the lithological map. This is expected because styles and density of fractures, and partially the alteration style, depend on rock type. To avoid this dependency and produce statistically robust WofE analyses, the lithological layer should be modified or used in a different way. Our results suggest that lithology should be used as restrictor instead of predictor layer, because as such, the information conveyed by that layer would be used for the prospectivity mapping but not in the statistical analysis. In addition, this practice proved to have strong influence in the area reduction. The restriction by favourable lithology is a reasonable practice because it is known a priori that lithologies deposited after the events of epithermal mineralization cannot host this type of mineralization.

However, there are two caveats for using the lithological layer to restrict the study area. Favourable lithologies and mineralized rocks are sometimes masked by thin layers of unfavourable lithology (young gravels or basalts) like in the San José district (Dietrich et al., 2012; Shatwell et al., 2011). Therefore, some areas discarded based on lithology alone may still contain mineralization beneath unfavourable lithologies. Other than field evidence, large (reactivated) structures may be the only indication of prospective ground underneath unfavourable lithologies. The regional-scale structural zones used for regional-scale mapping may provide that indication when the structures were reactivated or their detection is not totally hindered by younger deposits. The other caveat is that low accuracy of the lithological maps may lead to erroneous determinations. This may result in discarding areas that otherwise may be favourable, or may cause training deposits to be erroneously left out of the WofE calculations. This modifies the spatial associations between deposits and the other evidence layers.

Our results suggest that predictive mapping with the district-scale model in favourable areas, already delineated by our regional-scale predictive model, seems a reasonable practice to sequentially concentrate exploration efforts, mainly if the initial prospective areas have regional-scale dimensions. This is consistent with the sequential approach commonly carried out during mineral exploration. In addition, this approach is logical and feasible if we consider the differences in area reduction produced by the regional and district-scale models. In the district-scale area however, 3.3% of the areas predicted as unfavourable by the regional-scale dataset, are predicted as favourable by the district-scale model. This suggests a percentage of potentially mineralized areas that could be discarded if the predictive mapping is applied sequentially, or if the district-scale model is not applied at all. Therefore, the more effective approach may include the use of both mapping models in parallel, as independent tools.

5.2. Regional-scale vs. district-scale prospectivity mapping

Some advantages of the district-scale model over the regional-scale model for mapping districts or smaller areas include: a) its higher efficiency, which is suggested by the success-rate and prediction-rate of the favourability maps; b) the stronger spatial associations of LISEDs with the district-scale evidence layers, interpreted from slightly higher values of *C* in the district-scale model; c) higher conditional independence for district-scale evidence layers, which indicates that the absolute posterior probabilities yielded by the district-scale model are more reliable than those from the regional-scale model; d) the higher levels of detail and spatial resolution; and e) the much higher reduction of favourable area. While the district-scale model indicates as favourable only 12.7% of the district-scale area, the regional-scale model indicates as favourable 57.1% of the same area. The latter is even larger than the area covered by only the favourable lithology of

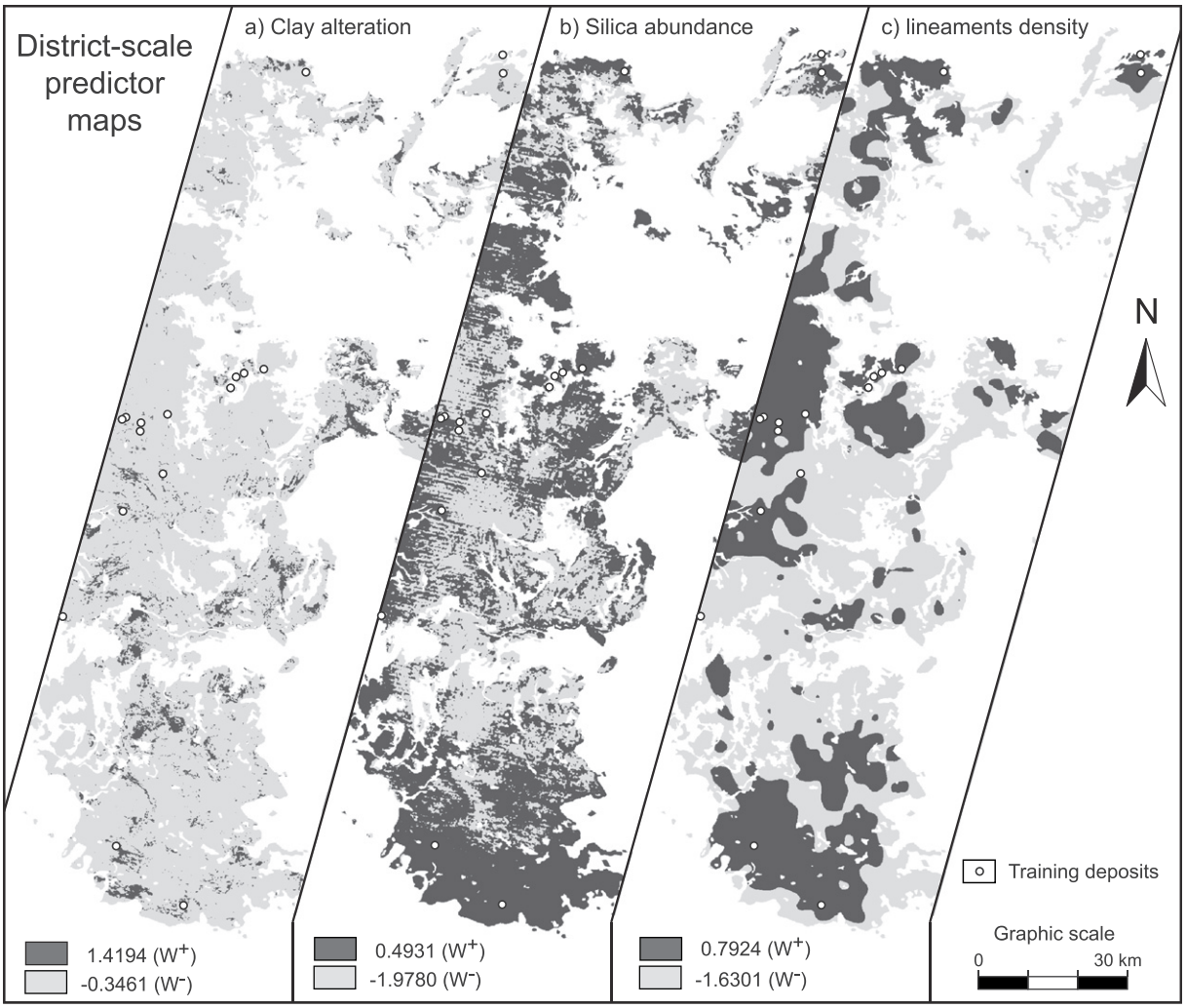

Fig. 6. Binary predictor maps representing the generalization of cumulative percentile evidence classes (Table 5) into two classes with predictor patterns present and absent, which are awarded the values of W^+ and W^- respectively. Dark grey shows the predictor patterns present.

the detailed lithological map (44% of the district-scale area). Considering only the area of favourable lithology in the detailed lithological map (5260.54 km^2), the regional-scale model reduced the potentially favourable areas to 83.8% of the initial area, while the district-scale model reduced it to only 28.9% of the same area. This indicates a higher usefulness of the district-scale model, because the aim of prospectivity mapping is to focus on favourable areas for follow up exploration.

These slightly more useful and efficient results of the district-scale model may be a consequence of using ASTER instead of Landsat, more accurate and detailed geological maps, and therefore higher resolution predictor maps. ASTER allowed including silica abundance as evidence, which had a beneficial influence in prospectivity mapping because silicification is one of the predominant type of alteration in this type of deposits in the Deseado Massif. In addition, the higher spectral resolution of ASTER may help to detect only the clay alteration minerals that predominate close to the mineralization. The higher spatial resolution of predictor maps in the district-scale model, permits higher details in the final maps, and the inclusion of small areas with favourable lithologies in the calculations. This avoids losing prospective ground and assures that most of the available deposits are used in the analysis. In the regional-scale model, the coarser spatial resolution of predictor maps and lower detail and accuracy of lithological evidence causes the areal extent of some formations (e.g., La Modesta) to become almost negligible in the calculations at regional-scale, because of the restricted size of their outcrops.

Potential disadvantages of district-scale models in the Deseado Massif are the limited availability of some data, the limited quality of available data, and the more demanding data processing. As well as in other regions of the world (Ford and Hart, 2013), data availability and quality are restricted in the Deseado Massif; the relatively low accuracy of available geological maps is an example of that. Positioning errors estimated for the geological maps used in this research are well above those recommended by the National Map Accuracy Standards of 1947 (U.S. Bureau of the Budget, 1947). This standard recommends that no more than 10% of the tested points should exceed an error of ~127 m for 1:250,000 scale maps and ~381 m for 1:750,000 scale maps, while the medians of errors for our geological maps are 268 and 1249 m for the respective scales. The use of ASTER involves a more demanding data processing and the difficulty of combining several scenes because of calibration differences.

5.3. Assessing the usefulness of evidence layers and improving the prospectivity mapping

Results of the predictive modelling procedures helped to assess the usefulness of the different types of evidence used in this research, and to infer which of them should be further investigated for improving the predictive models. Those investigations may include new exercises of prospectivity mapping as well as studies in specific subjects related to ore deposits geology.

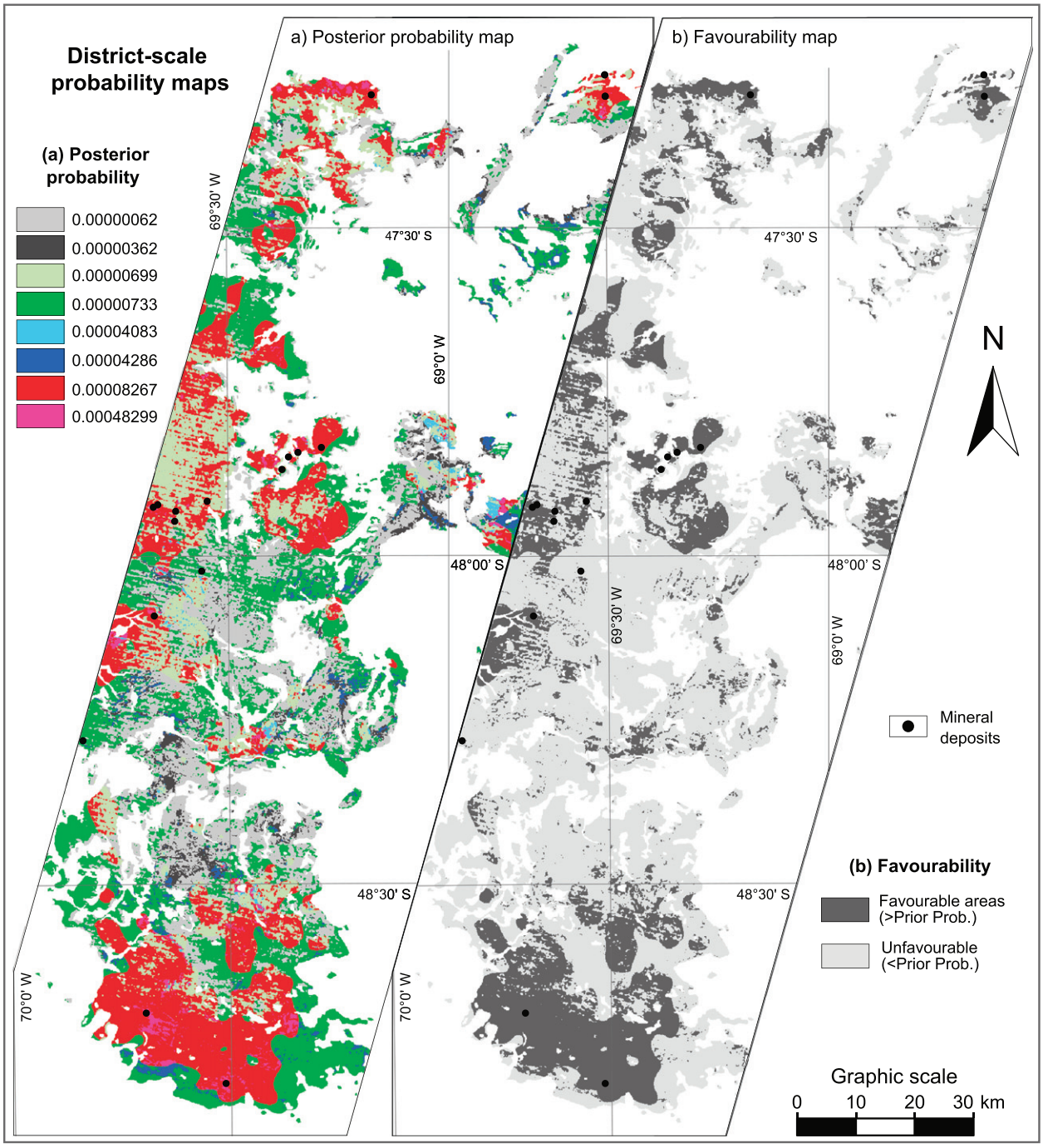

Fig. 7. District-scale probability maps. (a) Posterior probability map of LISEDs occurrence, showing the eight discrete classes of posterior probability produced by the WofE statistical calculations. (b) Favourability map for LISEDs occurrence.

Table 6
Confusion matrix derived from cross operation of regional- and district-scale favourability maps, in areas of favourable lithology of the district-scale area. Values are number of 100x100m cells in the maps.

		District-scale map			
		Favourable	Unfavourable	Total	
Regional-scale map	Favourable	135,040	305,891	440,931	83.8%
	Unfavourable	17,028	68,095	85,123	16.2%
Total	152,068	373,986	526,054		
	28.9%	71.1%			

The results of the spatial association analyses indicate that lithology, structures and silica abundance are effective spatial predictors. At regional-scale, both the lithological and the structural evidence show strong spatial associations with LISEDs. At district-scale, density of lineaments (indicative of fracturing and overall permeability), and K_{silica} index (indicative of silica abundance), showed strong spatial association and low W^- values. This suggested that most district-scale fractures mapped in this study were probably contemporaneous or older than the mineralization, and that areas with low density of fractures and no silicic alteration are less favourable to find LISEDs. In addition, the relatively large distance from regional structures (12,000 m) to reach the optimal spatial association with the LISEDs, may indicate that at least part of the mineralized rocks are hosted in secondary structures around

the regional structures. This may have been a consequence of the interaction of regional NNW-NW structures, which may have acted as fluid pathways, with other sets of structures (Giacosa et al., 2010), or with strongly fractured (permeable) rocks.

These strong associations confirm the importance of structural control on the emplacement of LISEDs in the Deseado Massif, as indicated by field studies of several authors (e.g., Dietrich et al., 2012; Echavarría et al., 2005; Fernández et al., 2008; Moreira et al., 2008; Schalamuk et al., 1997). It was also observed that siliceous alterations were strongly related with the mineralizing processes, and that these zones formed excellent features for deposit recognition in the area, as stated by Schalamuk et al. (2002).

Clay alteration layers used in this research are the weakest layers of evidence, which is consistent with results of Carranza and Andrada de Palomera (2005), but is contrasting with the conspicuous presence of clay alterations described in epithermal systems (Andrada de Palomera et al., 2012; Gemmell, 2007; Hedenquist et al., 2000; Simmons and Browne, 2000; Simmons et al., 2005; Simpson and Mauk, 2011; Zhai et al., 2009). Presence of clay alteration was amongst the best predictors in studies by other authors (e.g., Raines, 1999). These layers show the lowest contrasts in the spatial association analysis at regional- and district-scales. At district-scale, only about 35% of the deposits are located in areas with optimum spatial association of the clay alteration predictor map, and about 41% of the deposits are in cumulative classes with low *C*, suggesting that many deposits are located in areas where clay alteration was either absent or not detected. A possible explanation is that clay alteration haloes related to these deposits are restricted in size. This has been confirmed in extensively altered areas where the spatial extent of clay alteration is very small.

This weak spatial association between deposits and clay alteration may also be due to: (a) clay occurrences in the study area that are genetically unrelated to hydrothermal alteration (e.g., transported or produced by weathering); (b) the kind of methods that were used to produce the clay alteration evidence and predictor maps, including filtering and resampling to relatively large cells (mainly at regional-scale). They may have caused removal of small alteration anomalies, weakening the spatial association with the deposits; and (c) predominance of siliceous alteration in the centre of the deposits (where training points are located), which may have obscured clay alteration. This is likely since most deposits include silicification and stockworks, and some of them (e.g., Bacon-Mina Martha and Bajo Pobre) are located in areas with low C of the 4/6 band ratio image and with relatively high silica content (in the K_{silica} image).

Therefore, the geological evidence representing hydrothermal clay alteration should be studied in more detail in the Deseado Massif in order to obtain better results in the prospectivity mapping.

The lack of detailed knowledge about the relationship between LISEDs and the composition and spatial configuration of alteration envelopes, the lack of alteration ground-truth to calibrate remote sensing data, and the relatively coarse spatial and spectral resolutions of the available remote sensing data are limiting factors for mineral prospectivity mapping of districts and smaller areas in the Deseado Massif.

Customization of exploration models for different parts of the Deseado Massif may lead to improve the prospectivity mapping at district or larger scales. The structural differences amongst different sectors of the Deseado Massif, which were already suggested by Giacosa et al. (2010) and Japas et al. (2013), and the differences of structural controls on mineralization inferred by Andrada de Palomera and Carranza (2005), support the idea of predominant structural controls with slightly different directions in different sectors of the Deseado Massif. Although the structural evidence is probably the clearer example of the need for local customization, considering differences in patterns and types of alterations, and determining in detail the ages of mineralization and volcanic rocks would probably help improving the predictions.

The determination of the temporal limit between favourable and unfavourable lithologies with higher resolution than that of a formation can improve the prospectivity mapping in districts or smaller areas. This is possible because of the short lifespan of hydrothermal systems, which allows placing the upper limit of the mineralizing events between members of a formation in the stratigraphic sequence, as it has been done in some areas of the Deseado Massif (Andrada de Palomera et al., 2012; Permuy Vidal et al., 2014). Then, this can be used for constraining more accurately the initial areas to be assessed with WofE or similar techniques.

Accuracy and spatial detail of the evidence maps, which depend partially on spatial resolution, impact on the quality of the prospectivity mapping. Because geographic data is scale-dependant (Goodchild, 2011), excessive detail in regional-scale evidence maps (i.e., showing features hardly distinguishable at that scale) may result in problems, such as: a) cluttering of maps by fragmentation of areas that would show homogeneous probabilities at smaller scales; b) difficulties with handling of more voluminous data of higher resolution maps; and c) inefficient use of resources related to the acquisition of more detailed data (during field campaigns) if the prospectivity maps result from upscaling of evidence maps. On the other hand, more detailed evidence maps are advantageous because they allow increased map accuracy and a more precise delineation of areas of favourable evidence. Thus, the necessary detail of the input data depends on the scale at which the final predictive map will be displayed, and should be in accordance with the size of the area to be prospected.

In addition to spatial resolution, the spectral resolution of the optical satellite data affects the modelling results. In the current study, the clay alteration evidence layer from Landsat ETM + was produced at lower spectral resolution than that derived from ASTER data. The lower spectral resolution of Landsat ETM + data causes less detail in the reflectance spectra that were used for the mapping of alteration mineralogy. Absorption in Landsat band 7 can be caused by a variety of alteration minerals, including illite, smectite, kaolinite, alunite and chlorite. Since ASTER imagery has a higher spectral resolution in the wavelength range of Landsat band 7, the ASTER imagery can be used to discriminate better between alteration minerals and map more accurately illite, smectite and kaolinite. Therefore, the use of Landsat data seems adequate for the regional-scale mapping, with 1000 m spatial resolution, but for the district-scale mapping with 100 m spatial resolution, ASTER is more suitable because it may focus alteration mapping to mainly the illite-kaolinite-smectite richer areas, which are better indicators of mineralisation than for instance chlorite.

Finally, although not tested in this research, geochemical and geophysical evidence are other layers that could be investigated and included in the predictive mapping models. Magnetic and radiometric data are potentially useful for detection of hidden structures and areas containing strongly altered rocks.

6. Conclusions

Prospectivity for low- and intermediate-sulfidation epithermal deposits was mapped successfully in most of the Deseado Massif, by using easily obtainable datasets, and applying the weights of evidence and the leave-one-out cross-validation methods, which allowed using all available deposits for training the model, as well as for validating it.

Prospecting for low- and intermediate-sulfidation epithermal deposits in districts or smaller areas with our district-scale model was more useful, effective and reliable than using the regional-scale model. That reflects the efficiency of using more accurate and detailed lithological maps, the incorporation of silica abundance layer of evidence, the higher spectral resolution of ASTER, and the use of lithology as restrictor evidence instead of as predictor evidence. It likely also reflects the higher resolution of the district-scale predictor maps in contrast to the regional-scale predictor maps (100 m vs. 1000 m). Therefore, it seems worthwhile to use the district-scale datasets for prospectivity mapping in districts or smaller areas in the Deseado Massif.

The most efficient practice to map mineral prospectivity for low- and intermediate-sulfidation epithermal deposits in the Deseado Massif, and probably other regions, is to sequentially apply a district-scale prospectivity model in areas already indicated as favourable by a regional-scale prospectivity model. It seems more effective, however, to apply both models as independent and additive prospective tools, to avoid dismissing prospective ground that may be discarded by the regional-scale model.

The district-scale prospectivity models can be improved by investigating, in every district, the relationships between predominant deposit styles and different types of geological evidence. Most of these investigations should probably focus on hydrothermal alterations and the ways they can be detected. However, the study of pathfinder elements, structural controls, and relative age between mineralization and host rocks, should also be helpful for improving our predictions.

In addition, the accuracy and detail of the geological maps are key factors for improving the prospectivity mapping in the Deseado Massif and probably other areas where low and intermediate-sulfidation epithermal deposits are sought.

Acknowledgements

The Faculty of Geo-Information Science and Earth Observation (ITC) of the University of Twente, Fomicruz S.E., and Cerro Vanguardia S.A., financially supported this study. We thank Professor Freek van der Meer for promoting this investigation, and Alok Porwal and two anonymous reviewers from Ore Geology Reviews for their constructive suggestions and corrections to the manuscript.

References

Abrams, M., Hook, S., Ramachandran, B., 2002. ASTER User Handbook, Version 2: Advanced Spaceborne Thermal Emission and Reflection Radiometer. Jet Propulsion Laboratory.

Agterberg, F., 2011. A modified weights-of-evidence method for regional mineral resource estimation. Nat. Resour. Res. 20, 95–101.

Agterberg, F.P., Cheng, Q., 2002. Conditional independence test for weights-of-evidence modeling. Nat. Resour. Res. 11 (4), 249–255.

Andrada de Palomera, R.P., Carranza, E.J.M., 2005. Analysis of spatial distribution of epithermal gold deposits in the Deseado Massif, Santa Cruz province. Actas XVI Congreso Geológico Argentino, 19–23 September 2005, La Plata, pp. 715–722.

Andrada de Palomera, P., van Ruitenbeek, F.J.A., van der Meer, F.D., Fernández, R., 2012. Geochemical indicators of gold-rich zones in the La Josefina epithermal deposit, Deseado Massif, Argentina. Ore Geol. Rev. 45, 61–80.

Asadi, H.H., 2000. The Zarshuran gold deposit model applied in a mineral exploration GIS in Iran. ITC Diss. Number 78, 190.

Austin, J.R., Blenkinsop, T.G., 2009. Local to regional scale structural controls on mineralisation and the importance of a major lineament in the eastern Mount Isa Inlier, Australia: review and analysis with autocorrelation and weights of evidence. Ore Geol. Rev. 35, 298–316.

Behnia, P., 2007. Application of radial basis functional link networks to exploration for Proterozoic mineral deposits in Central Iran. Nat. Resour. Res. 16, 147–155.

Boleneus, D.E., Raines, G.L., Causey, J.D., Bookstrom, A.A., Frost, T.P., Hyndman, P.C., 2001. Assessment method for epithermal gold deposits in northeast Washington State using weights-of-evidence GIS modeling. US Geological Survey, Open-File Report 01-501, p. 52.

Bonham-Carter, G.F., 1994. Geographic Information Systems for Geoscientists. Pergamon.

Bonham-Carter, G.F., Agterberg, F.P., Wright, D.F., 1989. Weights of evidence modeling: a new approach to mapping mineral potential. In: Agterberg, F.P., Bonham-Carter, G.F. (Eds.), Statistical Applications in the Earth Sciences. Geological Survey of Canada, Paper 89–9, pp. 171–183.

Carranza, E.J.M., 2002. Geologically-constrained mineral potential mapping (examples from the Philippines). ITC Publ. Number 86, 480.

Carranza, E.J.M., 2004. Weights of evidence modeling of mineral potential: a case study using small number of prospects, Abra, Philippines. Nat. Resour. Res. 13 (3), 173–187.

Carranza, E.J.M., Andrada de Palomera, R.P., 2005. Evidential belief mapping of epithermal gold potential in the Deseado massif, Santa Cruz Province, Argentina. Actas XVI Congreso Geológico Argentino, 19–23 September 2005, La Plata, pp. 451–458.

Carranza, E.J.M., Hale, M., 2000. Geologically constrained probabilistic mapping of gold potential, Bagio district, Philippines. Nat. Resour. Res. 9 (3), 237–253.

Carranza, E.J.M., Hale, M., 2001. Geologically constrained fuzzy mapping of gold mineralization potential, Baguio district, Philippines. Nat. Resour. Res. 10, 125–136.

Carranza, E.J.M., Hale, M., 2003. Evidential belief functions for data-driven geologically constrained mapping of gold potential, Baguio district, Philippines. Ore Geol. Rev. 22, 117–132.

Carranza, E.J.M., Sadeghi, M., 2010. Predictive mapping of prospectivity and quantitative estimation of undiscovered VMS deposits in Skellefte district (Sweden). Ore Geol. Rev. 38, 219–241.

Carranza, E.J.M., van Ruitenbeek, F.J.A., Hecker, C., van der Meijde, M., van der Meer, F.D., 2008. Knowledge-guided data-driven evidential belief modeling of mineral prospectivity in Cabo de Gata, SE Spain. Int. J. Appl. Earth Obs. Geoinformation 10 (3), 374–387.

Chung, C.F., Fabbri, A.G., 2003. Validation of spatial prediction models for landslide hazard mapping. Nat. Hazards 30, 451–472.

Cobos, J.C., Panza, J.L., 2003. Hoja Geológica 4769-I, El Pluma. Servicio Geológico Minero Argentino. Instituto de Geología y Recursos Minerales.

Coupland, T., 2009. Update Report on the Cerro Moro Project, Santa Cruz Province, Argentina. Technical Report (NI 43-101) prepared for Exeter Resource Corporation and Extorre Gold Mines Ltd.

Crósta, A., Moore, J.M., 1989. Enhancement of Landsat Thematic Mapper imagery for residual soil mapping in SW Minais Gerais State, Brazil: a prospecting case history in Greenstone belt terrain. 7th ERIM Thematic Conference: Remote Sensing for Exploration Geology, Calgary, Canada, pp. 1173–1187.

Davis, J.C., 1986. Statistics and Data Analysis in Geology. John Willey & Sons, New York.

de Barrio, R.E., Palma, R.M., Panza, J.L., 1986. Deseado Massif, correlation with the Andean region. In: The Geologic Evolution of South America, Servicio Geologico Minero Argentino. Unpublished.

de Barrio, R., Panza, J.L., Nullo, F., 1999. Jurásico y Cretácico del Macizo del Deseado, provincia de Santa Cruz. In: Caminos, R. (Ed.), Geología Argentina, anales 29. Instituto de Geología y Recursos Minerales, pp. 511–527.

De Giusto, J.M., Di Persia, C., Pezzi, E., 1980. Nesocratón del Deseado. Geología Regional Argentina, Academia Nacional de Ciencias, Córdoba, II, pp. 1389–1430.

de Quadros, T.P., Koppe, J., Strieder, A., Costa, J.C.L., 2006. Mineral-potential mapping: a comparison of weights-of-evidence and fuzzy methods. Nat. Resour. Res. 15, 49–65.

Deng, M., 2009. A conditional dependence adjusted weights of evidence model. Nat. Resour. Res. 18, 249–258.

Dietrich, A., Gutierrez, R., Nelson, E., Layer, P., 2012. Geology of the epithermal Ag–Au Huevos Verdes vein system and San José district, Deseado massif, Patagonia, Argentina. Mineral. Deposita 47, 233–249.

Dinger, J.S., Andrews, R.E., Wunsch, D.R., Dunno, G.A., 2002. Remote sensing and field techniques to locate fracture zones for high-yield water wells in the Appalachian Plateau, Kentucky. Proceedings of the National Ground Water Association Fractured-Rock Aquifer 2002 Conference, Denver, Colorado, pp. 195–199.

Echavarría, L., 2004. Los fluidos hidrotermales formadores de la mineralización epitermal el Dorado-Monserrat, Macizo del Deseado. Rev. Asoc. Geol. Argent. 59, 70–82.

Echavarría, L.E., Schalamuk, I.B., Etcheverry, R.O., 2005. Geologic and tectonic setting of Deseado Massif epithermal deposits, Argentina, based on El Dorado-Monserrat. J. S. Am. Earth Sci. 19 (4), 415–432.

Echeveste, H., 2010. Control estructural de la mineralización epitermal del distrito Manantial Espejo, Santa Cruz. Rev. Asoc. Geol. Argent. 66, 325–334.

Einaudi, M.T., Hedenquist, J.W., Inan, E.E., 2003. Sulfidation state of fluids in active and extinct hydrothermal systems: transitions from porphyry to epithermal environments. Soc. Econ. Geol. Spec. Publ. 10, 285–313.

Fernández, R.R., Echeveste, H., Echavarría, L., Schalamuk, I.B., 1996. Control volcánico y tectónico de la mineralización epitermal del área de La Josefina, Macizo del Deseado, Santa Cruz, Argentina. Actas XIII Congreso Geológico Argentino y III Congreso de Exploración de Hidrocarburos, Buenos Aires, III, pp. 41–54.

Fernández, R.R., Blesa, A., Moreira, P., Echeveste, H., Mykietiuk, K., Andrada de Palomera, P., Tessone, M., 2008. Los depósitos de oro y plata vinculados al magmatismo jurásico de la Patagonia: revisión y perspectivas para la exploración. Rev. Asoc. Geol. Argent. 63, 665–681.

Feruglio, E., 1949. Descripción geológica de la Patagonia (3 tomos). Yacimientos Petrolíferos Fiscales. Unpublished.

Ford, A., Hart, C.J.R., 2013. Mineral potential mapping in frontier regions: a Mongolian case study. Ore Geol. Rev. 51, 15–26.

Gemmell, J.B., 2007. Hydrothermal alteration associated with the Gosowong Epithermal Au–Ag Deposit, Halmahera, Indonesia: mineralogy, geochemistry, and exploration implications. Econ. Geol. 102 (5), 893–922.

Giacosa, R.E., César, O., Genini, A.D., 1998. Hoja Geológica 4766-III y IV, Puerto Deseado. Servicio Geológico Minero Argentino, Subsecretaría de Minería de la NaciónBoletín 240. Programa Nacional de Cartas Geológicas de la República Argentina (1:250,000).

Giacosa, R.E., Márquez, M.M., Panza, J.L., 2002. Basamento Paleozóico Inferior del Macizo del Deseado. In: Haller, M.J. (Ed.), Geología y Recursos Naturales de Santa Cruz. Relatorio XV Congreso Geológico Argentino, El Calafate I-2, pp. 33–44.

Giacosa, R., Zubia, M., Sánchez, M., Allard, J., 2010. Meso-Cenozoic tectonics of the Southern Patagonian foreland: structural evolution and implications for Au–Ag veins in the Eastern Deseado Region (Santa Cruz, Argentina). J. S. Am. Earth Sci. 30, 134–150.

Godeas, M.A., 1985. Geología del Bajo de La Leona y su mineralogía asociada, Provincia de Santa Cruz. Rev. Asoc. Geol. Argent. 40 (3–4), 262–277.

González Guillot, M., de Barrio, R., Ganem, F., 2004. Mina Martha: un Yacimiento epitermal argentífero en el Macizo del Deseado, provincia de Santa Cruz. Actas 7° Congreso de Mineralogía y Metalogenia, Río Cuarto, Argentina, pp. 199–204.

González-Álvarez, I., Porwal, A., Beresford, S.W., McCuaig, T.C., Maier, W.D., 2010. Hydrothermal Ni prospectivity analysis of Tasmania, Australia. Ore Geol. Rev. 38, 168–183.

Goodchild, M.F., 2011. Scale in GIS: an overview. Geomorphology 130, 5–9.

Grove, C.I., Hook, S.J., Paylor, E.D., 1992. Laboratory Reflectance Spectra For 160 Minerals 0.4–2.5 Micrometers. Jet Propulsion Laboratory (JPL), Publication, pp. 2–92.

Guido, D.M. 2002. Geología y Metalogénesis del Sector Oriental del Macizo del Deseado, provincia de Santa Cruz. Tesis Doctoral, Facultad de Ciencias Naturales y Museo, Universidad Nacional de La Plata, (inédita), 226 p.

Guido, D., 2004. Caracterización de los fluidos hidrotermales en el área Chispas, este del Macizo del Deseado, provincia de Santa Cruz. 7° Congreso de Mineralogía y Metalogenia, pp. 213–218.
Guido, D.M., Jovic, S.M., Schalamuk, I.B., 2005. A new metallogenical association (Sn–Cd–In–Zn–Ag–Au) in the Deseado auroargentiferous province, Deseado Massif, Patagonia, Argentina. In: Mao, J., Bierlein, F.P. (Eds.), Mineral Deposit Research: Meeting the Global Challenge. Springer, Berlin Heidelberg, pp. 965–968.
Gust, D.A., Biddle, K.T., Phelps, D.W., Uliana, M.A., 1985. Associated middle to late Jurassic volcanism and extension in southern South America. Tectonophysics 116, 223–253.
Harris, D., Pan, G., 1999. Mineral favorability mapping: a comparison of artificial neural networks, logistic regression, and discriminant analysis. Nat. Resour. Res. 8, 93–109.
Harris, J.R., Sanborn-Barrie, M., 2006. Mineral potential mapping: examples from the Red Lake Greenstone Belt, Northwest Ontario. In: Harris, J.R. (Ed.), GIS Applications in Earth Sciences. Special Publication 44. Geological Association of Canada, pp. 1–22.
Hedenquist, J.W., Arribas, A.R., González-Urien, E., 2000. Exploration for epithermal gold deposits. In: Hagemann, S.G., Brown, P.E. (Eds.), Gold in 2000. Society of Economic Geologists, Reviews in Economic Geology 13, pp. 245–277.
Hung, L.Q., Batelaan, O., De Smedt, F., 2005. Lineament extraction and analysis, comparison of LANDSAT ETM and ASTER imagery. In: Ehlers, V.M., Ulrich, M. (Eds.), Case study: Suoimuoi Tropical Karst Catchment, Vietnam. Remote Sensing for Environmental Monitoring, GIS Applications, and Geology 5983. V Proceedings of SPIE, Bellingham, WA, 5983, pp. 182–193.
Japas, M.S., Sruoga, P., Kleiman, L.E., Gayone, M.R., Maloberti, A., Comito, O., 2013. Cinemática de la extensión jurásica vinculada a la Provincia Silícea Chon Aike, Santa Cruz, Argentina. Rev. Asoc. Geol. Argent. 70, 16–30.
John, D.A., 2001. Miocene and early Pliocene epithermal gold–silver deposits in the northern Great Basin, western United States: characteristics, distribution, and relationship to Magmatism. Econ. Geol. 96, 1827–1853.
Jovic, S., Guido, D.M., Tiberi, P., Schalamuk, I.B., 2004. Cerro León, una variación del modelo epitermal de baja sulfuración del Macizo del Deseado. Actas 7° Congreso de Mineralogía y Metalogenia, Río Cuarto, Argentina, pp. 225–230.
Jovic, S., Guido, D., Schalamuk, I., Ríos, F., Tassinari, C., Recio, C., 2011. Pingüino In-bearing polymetallic vein deposit, Deseado Massif, Patagonia, Argentina: characteristics of mineralization and ore-forming fluids. Mineral. Deposita 46 (3), 257–271.
Koike, K., Nagano, S., Ohmi, M., 1995. Lineament analysis of satellite images using a Segment Tracing Algorithm (STA). Comput. Geosci. 21, 1091–1104.
Lepage, R., Rouhana, R.G., St-Onge, B., Noumeir, R., Desjardins, R., 2000. Cellular neural network for automated detection of geological lineaments on Radarsat images. IEEE Trans. Geosci. Remote Sens. 38, 1224–1233.
Lesta, P.J., Ferello, R., 1972. Región extraandina de Chubut y norte de Santa Cruz. Geología Regional Argentina. Academia Nacional de Ciencias, pp. 601–654.
Marjoribanks, R., 2010. Geological methods in mineral exploration and mining. 2nd ed. Springer-Verlag, Berlin Heidelberg.
Márquez, M.J., Giacosa, R.E., Godeas, M.A., 2002. Los Granitoides gondwánicos del borde oriental del Macizo del Deseado. In: Haller, M.J. (Ed.), Relatorio XV Congreso Geológico Argentino, El Calafate. Geología y Recursos Naturales de Santa Cruz I-4, pp. 57–70.
Miyatake, S., 2002. Regional lineament analysis and alteration mineral mapping for intrusive-related copper exploration in the Myanmar central volcanic belt. 23rd Asian Conference on Remote Sensing (papers on-line). GIS development, Katmandu (4 pp.).
MMAJ, 2000. Technical development report: examination of indices for discriminating rocks and minerals and their universal validity (In Japanese with English abstract). Metall. Min. Agency Jpn. III, 1–31.
Moon, C.J., Whateley, M.K.G., Evans, A.M., 2006. Introduction to Mineral Exploration. 2nd ed. Blackwell Publishing.
Moor, D.S., McCabe, G.P., 1999. Introduction to the Practice of Statistics. W.H. Freeman and Company, New York.
Moreira, P. 2005. Geología y metalogénesis del prospecto La Josefina, Macizo del Deseado, provincia de Santa Cruz. Tesis doctoral, Facultad de Ciencias Naturales y Museo, Universidad Nacional de La Plata, (inédita), 360 p.
Moreira, P., Fernández, R., Ríos, J., Schalamuk, I.A., 2004. Caracterización de la esfalerita de las manifestaciones epitermales del área La Josefina, Macizo del Deseado, Provincia de Santa Cruz. Actas VII Congreso de Mineralogía y Metalogenia, Río Cuarto (Córdoba), pp. 89–94.
Moreira, P., Fernández, R., Cabana, C., Schalamuk, I., 2008. Análisis estructural de las mineralizaciones jurásicas del proyecto epitermal La Josefina (Au–Ag), Macizo del Deseado, Santa Cruz. Rev. Asoc. Geol. Argent. 63 (2), 244–253.
Mykietiuk, K., Fernández, R., Azevedo, F., 2005. Alteraciones hidrotermales superpuestas: producto de fluidos de pH neutro y ácido en el cerro Guanaco, Macizo del Deseado, Santa Cruz. Rev. Asoc. Geol. Argent. 60, 23–31.
Dirección Nacional del Servicio Geológico, 1994. Mapa Geológico de la Provincia de Santa Cruz (escala 1:750,000), República Argentina. Dirección Nacional del Servicio Geológico, Secretaría de Minería.
Nelson, E.P., Dalziel, I.W.D., Milnes, A.G., 1980. Structural geology of the Cordillera Darwin collisional-style orogenesis in the southernmost Chilean Andes. Zeitschrift: Eclogae Geologicae Helvetiae 73 (3), 727–751.
Nykänen, V., Ojala, V.J., 2007. Spatial analysis techniques as successful mineral-potential mapping tools for orogenic gold deposits in the northern Fennoscandian Shield, Finland. Nat. Resour. Res. 16, 85–92.
Páez, G.N., Ruiz, R., Guido, D.M., Jovic, S.M., Schalamuk, I.B., 2011. Structurally controlled fluid flow: high-grade silver ore-shoots at Martha epithermal mine, Deseado Massif, Argentina. J. Struct. Geol. 33, 985–999.
Panza, J.L., 1982. Descripción geológica de las Hojas 53e "Gobernador Moyano" y 54e "Cerro Vanguardia". Servicio Geológico Minero Argentino. Unpublished.
Panza, J.L., 1994a. Hoja Geológica 4969 - II, Tres Cerros, Provincia de Santa Cruz. Dirección Nacional del Servicio Geológico, Programa Nacional de Cartas Geológicas de la República Argentina (1:250000)Boletín 213.
Panza, J.L., 1994b. Hoja Geológica 4966 - I y II, Bahía Laura, Provincia de Santa Cruz. Dirección Nacional del Servicio Geológico, Programa Nacional de Cartas Geológicas de la República Argentina (1:250000)Boletín 214.
Panza, J.L., 2001. Hoja Geológica 4769-IV Monumento Natural Bosques Petrificados, Provincia de Santa Cruz. Servicio Geológico Minero Argentino, Programa Nacional de Cartas Geológicas de la República Argentina (1:250000)Boletín 258.
Panza, J.L., Cobos, J.C., 2001. Hoja Geológica 4769-III, Destacamento La Maria. Servicio Geológico Minero Argentino, Programa Nacional de Cartas Geológicas de la República Argentina (1:250000)Boletín 296.
Panza, J.L., Marín, G., 1998. Hoja Geológica 4969-I, Gobernador Gregores. Servicio Geológico Minero Argentino, Programa Nacional de Cartas Geológicas de la República Argentina (1:250000)Boletín 239.
Permuy Vidal, C., Paez, G.N., Guido, D.M., Jovic, S.M., Ruiz, R., 2014. Vulcanismo pre, sin y post-mineral en el distrito epitermal Cerro Negro (Au–Ag), Macizo del Deseado, Provincia de Santa Cruz. XIX Congreso Geológico Argentino, Córdoba (2 pp.).
Porwal, A., Carranza, E.J.M., Hale, M., 2003. Knowledge-driven and data-driven fuzzy models for predictive mineral potential mapping. Nat. Resour. Res. 12, 1–25.
Porwal, A., Carranza, E.J.M., Hale, M., 2006. Bayesian network classifiers for mineral potential mapping. Comput. Geosci. 32, 1–16.
Porwal, A., González-Álvarez, I., Markwitz, V., McCuaig, T.C., Mamuse, A., 2010. Weights-of-evidence and logistic regression modeling of magmatic nickel sulfide prospectivity in the Yilgarn Craton, Western Australia. Ore Geol. Rev. 38, 184–196.
Prakash, A., 2001. Radiometric aspects. In: Janssen, L.L.F., Huurneman, G.C. (Eds.), Principles of Remote Sensing. ITC Educational Textbook Series, International Institute for Aerospace Survey and Earth Sciences (ITC), Chapter 8.
Raines, G.L., 1999. Evaluation of weights of evidence to predict epithermal-gold deposits in the Great Basin of the Western United States. Nat. Resour. Res. 8 (4), 257–276.
Ramos, V.A., 2002a. Evolución Tectónica. In: Haller, M.J. (Ed.), Geología y Recursos Naturales de Santa Cruz. Relatorio XV Congreso Geológico Argentino, El Calafate, pp. 1–23.
Ramos, V.A., 2002b. El magmatismo paleógeno de la Cordillera Patagónica. In: Haller, M.J. (Ed.), Relatorio XV Congreso Geológico Argentino. Geología y Recursos Naturales de Santa Cruz, El Calafate, pp. 165–174.
Reimer, W., Miller, H., Mehl, H., 1996. Mesozoic and Paleozoic Paleo-stress fields of the South Patagonian Massif deduced from structural and remote sensing data. In: Storey, B.C., King, E.C., Livermore, R.A. (Eds.), Weddell Sea tectonics and Gondwana break-up. Geological Society Special Publication 108, pp. 73–85.
Rios, F.J., Alves, J.V., Fuzikawa, K., Schalamuk, I.A., de Barrio, R., del Blanco, M., 2000. Fluid evolution in the La Josefina Au-epithermal system, Macizo del Deseado, southern Patagonia, Santa Cruz, Argentina. Revista Brasileña de Geociencias 30, 769–774.
Rolando, A.P., Fernández, R.R., 1996. Alteración hidrotermal del sector nor-oriental del prospecto epitermal La Josefina, Santa Cruz. III Reunión de Mineralogía y Metalogenia, La Plata, pp. 209–216.
Sabins, F.F., 1999. Remote sensing for mineral exploration. Ore Geol. Rev. 14, 157–183.
Sandefur, R.L., 2007. Lomada Leiva Project, Santa Cruz province, Argentina. Technical Report (NI 43-101) prepared for Patagonia Gold Plc.
Sanders, G., 2000. Regional geologic setting of the gold-silver veins of the Deseado Massif, Southern Patagonia, Argentina. Argentina Mining 2000: Exploration, Geology, Mine Development and Business Opportunities Conference, Engineering and Mining Journal and LatinoMineria, Mendoza.
Sawatzky, D.L., Raines, G.L., Bonham-Carter, G.F., Looney, C.G., 2009. Spatial Data Modeller (SDM): ArcMAP 9.3 geoprocessing tools for spatial data modelling using weights of evidence, logistic regression, fuzzy logic and neural networks. http://arcscripts.esri.com/details.asp?dbid=15341.
Schalamuk, I.B., Zubia, M., Genini, A., Fernandez, R.R., 1997. Jurassic epithermal Au–Ag deposits of Patagonia, Argentina. Ore Geol. Rev. 12 (3), 173–186.
Schalamuk, I.B., de Barrio, R.E., Zubia, M., Genini, A., Echeveste, H., 1999. Provincia auroargentífera del Deseado, Santa Cruz. In: Zappettini, E. (Ed.), Recursos Minerales de la República Argentina. Servicio Geológico Minero Argentino, pp. 1178–1188.
Schalamuk, I.B., de Barrio, R.E., Zubia, M.A., Genini, A., Valvano, J., 2002. Mineralizaciones auroargentíferas del Macizo del Deseado y su encuadre metalogénico, Provincia de Santa Cruz. In: Haller, M.J. (Ed.), Geología y Recursos Naturales de Santa Cruz. Relatorio XV Congreso Geológico Argentino, El Calafate, pp. 679–713.
Shatwell, D., Clifford, J.A., Echavarria, D., Irusta, G., Lopez, D., 2011. Discoveries of low-sulfidation epithermal Au–Ag veins at Cerro Negro, Deseado Massif, Argentina. Society of Economic Geologists, Newsletterp. 85.
Sillitoe, R.H., Hedenquist, J.W., 2003. Linkages between volcanotectonic settings, ore–fluid compositions, and epithermal precious metal deposits. Soc. Econ. Geol. Spec. Publ. 10, 315–343.
Simmons, S.F., Browne, P.R.L., 2000. Hydrothermal minerals and precious metals in the Broadlands-Ohaaki geothermal system: implications for understanding low-sulfidation epithermal environments. Econ. Geol. 95 (5), 971–999.
Simmons, S.F., White, N.C., John, D.A., 2005. Geological characteristics of epithermal precious and base metal deposits. Economic Geology 100 th Anniversary Volume, pp. 485–522.
Simpson, M.P., Mauk, J.L., 2011. Hydrothermal alteration and veins at the epithermal Au–Ag deposits and prospects of the Waitekauri Area, Hauraki Goldfield, New Zealand. Econ. Geol. 106 (6), 945–973.
Singer, D., Kouda, R., 1999. A comparison of the weights-of-evidence method and probabilistic neural networks. Nat. Resour. Res. 8, 287–298.
Snedecor, G.W., Cochran, W.G., 1967. Statistical Methods. 6th ed. Iowa State University Press.
Somoza, R., Vizán, H., Taylor, G.K., 2008. Tectonic rotations in the Deseado Massif, southern Patagonia, during the breakup of Western Gondwana. Tectonophysics 460, 178–185.
Uliana, M.A., Biddle, K.T., Phelps, D.W., Gust, D.A., 1985. Significado del vulcanismo y extensión mesojurásicos en el extremo meridional de Sudamérica. Rev. Asoc. Geol. Argent. 40 (3–4), 231–253.

U.S. Bureau of the Budget, 1947. United States National Map Accuracy Standards. U.S. Bureau of the Budget, Washington, D.C.
Varela, R., Pezzuchi, H., Genini, A., Zubia, M., 1991. Dataciones de rocas magmáticas en el Jurásico inferior del nordeste del Macizo del Deseado, Santa Cruz. Rev. Asoc. Geol. Argent. 46 (3–4), 257–262.
White, N.C., Hedenquist, J.W., 1990. Epithermal environments and styles of mineralization: variations and their causes, and guidelines for exploration. J. Geochem. Explor. 36 (1–3), 445–474.
Zhai, W., Sun, X., Sun, W., Su, L., He, X., Wu, Y., 2009. Geology, geochemistry, and genesis of Axi: a Paleozoic low-sulfidation type epithermal gold deposit in Xinjiang, China. Ore Geol. Rev. 36 (4), 265–281.
Zubia, M., Genini, A., 2003. Yacimientos auroargentíferos epitermales del Macizo del Deseado, Provincia de Santa Cruz. Serie Contribuciones Técnicas, Recursos Minerales 13/D. Servicio Geológico Minero Argentino (SEGEMAR).
Zubia, M.A., Genini, A.D., Schalamuk, I.B., 1999. Yacimiento Cerro Vanguardia, Santa Cruz. In: Zappettini, E. (Ed.), Recursos Minerales de la República Argentina. Servicio Geológico Minero Argentino, Anales 35, pp. 1189–1202 (T II).